

How negative feedback from filamentous actin affects cell shapes and motility

Jack M. Hughes^{*1}, Jupiter Algorta², and Leah Edelstein-Keshet²

¹Department of Mathematics and Statistics, Concordia University, Montreal, QC, Canada

²Department of Mathematics, University of British Columbia, Vancouver, BC, Canada

February 10, 2026

Abstract

The crawling motility of many eukaryotic cells is driven by filamentous actin (F-actin), and regulated by a network of signaling proteins and lipids (including small GTPases). The tangle of positive and negative feedback loops gives rise to various experimentally observed dynamic patterns (“actin waves”). Here we consider a recent prototypical model for actin waves in which F-actin exerts negative feedback onto a GTPase. Guided by recent numerical PDE bifurcation analysis in [25, 27], we explore cell shapes and motility associated with polar, oscillatory, and traveling waves solutions of a mass-conserved partial differential equation (PDE) model. We use Morpheus (cellular Potts) simulations to investigate the implications of such regimes of behavior on the shapes and motion of cells, and on transitions between modes of behavior. The model demonstrates various cell states, including resting (spatially uniform GTPase), polar cells (static “zones” of GTPase), and traveling waves along the cell edge. In some parameter regimes, such states can coexist, so that cells can transition from one behavior to another in response to noisy stimuli.

1 Introduction

Understanding eukaryotic cell motility continues to be one of the grand challenges of modern cell biology, engendering both experimental and theoretical research. Experimentally, many complex cell motility modes have been observed in a wide variety of cell types [7, 37, 40, 52]. Commonly, cells experience directed cell motion, which is key in many biological processes including cancer metastasis [47] and wound healing [55, 58]. Other modes of motility can also occur such as random amoeboid-type motion, and cell turning and ruffling. Among the fundamental questions to be addressed, we ask how cell motility is regulated and what causes cells to change motility modes.

While new mechanisms powering cell motility are continually being discovered, the leading role of filamentous actin (F-actin) is well-recognized in basic directed migration of neutrophils, keratocytes, social amoeba (*Dictyostelium discoideum*) and other cell types. F-actin is a key player in cell motility because the “barbed ends” of these filaments, at which actin monomers assemble, accumulate near the front edge of a cell and cause the edge to protrude outwards. However, it is not always clear what interactions between F-actin and its regulators are at the core of the complex motility machinery. Our interest here is in accounting for basic cell motility patterns such as directed motion, turning, ruffling, and random motility. We consider a small subset of the central signaling network, consisting of a small GTPase (such as Rho, Rac, or Cdc42) (Figure 1a) and the interaction with F-actin.

GTPases act as molecular switches, with the active form bound to the membrane and the inactive in the cell interior (cytosol). The activation and inactivation of these GTPases are on the scale of seconds/minutes, while any loss or production is on a much longer scale [34]. This justifies the common modeling assumption that the total quantity of a given GTPase is conserved over the timescale of interest for motile cells (minutes). The conversion from inactive to active form is governed by GEFs (guanine nucleotide exchange factors) and the reverse by GAPs (GTPase-activating proteins). The patterns induced by these Rho-GTPases dictate the distribution of F-actin.

^{*}Corresponding author
Email address: jack.hughes@mail.concordia.ca

Recent experimental evidence shows that F-actin is not only governed by Rho GTPases but, in certain cells, it can also affect the activity of the GTPase. Feedback between GTPases and F-actin results in a variety of experimentally observable dynamic patterns, commonly denoted “actin waves” [4, 6, 7, 9, 10, 12, 17, 19, 20, 31, 39, 36, 54, 59]. For example, F-actin can promote GTPase inactivation by recruiting GAPs [8] (Figure 1b). This negative feedback loop leads to many interesting actin wave structures and forms the basis of the actin waves modeling in this paper. Experimental work shows a rich structure of waves along the cell edge, including oscillatory waves [20], traveling waves along the cell front [7] and waves on the cell membrane [60, 38]. Thus, these wave-like dynamics appear in many different settings, although the proposed mechanisms governing these patterns vary. A key motivation of our work is to explore how these actin waves affect cell motility.

Models describing actin waves tend to be complex, often relying on numerical simulations alone to understand model behavior. Such studies favor model details over unraveling generic model structure. It can be challenging to fully understand the results. Using simulations alone can also miss important parameter regimes where there is coexistence of different behaviors or transitions from one behavior to another. In this work, we leverage a previous study that analyzed a simple reaction-diffusion (RD) model for actin waves [27]. There, numerical bifurcation analysis was used to identify a mathematical mechanism for coexistence of polar patterns (with a clear front and back) and multi-peak traveling waves suspected to lead to directed cell motion and cell ruffling, respectively. In particular, a parameter regime was identified where such patterns are stable and coexist. Other works in which numerical bifurcation analysis has been used to study actin waves models include [10, 61]. Here, our key motivation is to then determine what types of cell shapes and motility occur based on the structures identified by [27].

The intracellular dynamics of actin waves only provides part of the picture at the cell-scale. To understand how actin waves affect cell shape and motility, the dynamics must be coupled to a model for cell deformations. Common techniques for capturing deformable cell domains include Lagrangian marker point, level set methods [43], phase field methods [46, 15, 5], finite elements [16, 18], and Metropolis-based methods including the cellular Potts model (CPM) [3]. Additional references using such methods can be found in the reviews by [1, 11, 13, 14, 24, 48, 50]. The goal of the present study is to provide a simple, reproducible connection between the reaction-diffusion dynamics and cell deformations so that cell-scale structures can be studied. Therefore, we use the CPM framework [22], as this is arguably the simplest [2] and can be easily implemented using the open source software package Morpheus [49]. For the basics on the CPM framework, see Section B.

Many previous papers have described dynamic cell shapes using the CPM formalism, and many of those papers have included PDEs for the proteins that regulate F-actin and cell motion. Examples include [35, 32, 44]. These examples are more advanced in that they simulated PDEs inside fully 2D deforming cell domains. However, none of these works had accompanying PDE bifurcation analysis, nor did they attempt to map out the mechanisms for transitions between multiple observed cell behaviors. Also, since previous simulations were done with custom-made proprietary codes, reproducing previous results, or building upon them, remains challenging.

To address these issues, we use the open source simulation platform Morpheus, together with the numerical bifurcation analysis by [25, 27]. To investigate cell shape and motility, we construct initial conditions and choose parameter values near key locations along the solution branches. We depict cell shapes using CPM simulations, where outward protrusion updates are favored in areas with high F-actin concentration. Our results demonstrate transitions between directed cell motion, cell turning, and ruffling based on the intracellular dynamics of actin waves.

2 Methods

2.1 The signaling model

The model of interest consists of two underlying subsystems. The first is the main regulatory unit (e.g. Rho GTPase) whose active (u) and inactive (v) forms satisfy overall mass conservation (Figure 1a). This subsystem, denoted “wave-pinning” was studied by [41] as a model for cell polarization: the PDE model supports a stable pattern with a zone of high Rho activity under appropriate conditions. The second subsystem, F-actin (F) is promoted by the GTPase, and provides negative feedback that enhances the inactivation of the GTPase (Figure 1b). Similar circuits have been modeled in both theoretical [23, 32] and experiment-modeling papers [9, 21, 31, 39, 51] (see Section A.3 for more details).

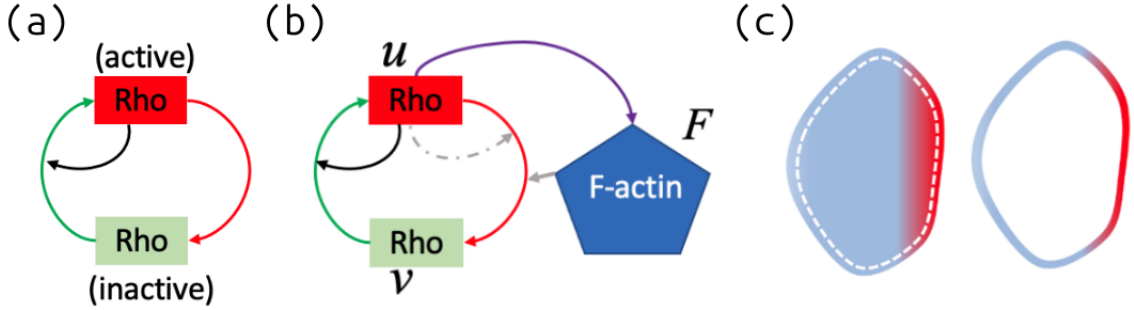


Figure 1: **Schematic diagram of models:** (a) Typical cycling between active (red) and inactive (green) Rho GTPase with positive feedback from the active form to its own activation. The model by [41] for polarization (“wave-pinning”, WP) was based on this circuit. (b) A downstream effector (such as F-actin) is promoted by the GTPase, and then exerts negative feedback (enhances the inactivation of Rho). Arrow colors represent GAP (red), GEF (green), downstream target (purple), positive (solid black) and negative (gray) feedback. The dot-dashed gray arrow in (b) was proposed as a simplification of the saturating kinetics used in [23]. (c) The distribution of active GTPase on a thin sheet-like cell has been simulated elsewhere in 2D (e.g., in [35]). Here, our geometry is a periodic 1D domain along the cell edge (white dashed curve, and contour shown on the right).

We model the uvF system using the dimensionless set of partial differential equations

$$\frac{\partial u}{\partial t} = (b + \gamma u^2)v - (1 + sF + u^2)u + D_u u_{xx}, \quad (1a)$$

$$\frac{\partial v}{\partial t} = -(b + \gamma u^2)v + (1 + sF + u^2)u + D_v v_{xx}, \quad (1b)$$

$$\frac{\partial F}{\partial t} = \omega(p_0 + p_1 u - F) + D_F F_{xx}, \quad (1c)$$

in one spatial dimension (1D) with periodic boundary conditions on the domain $(0, 1)$ to represent the edge of a cell (see Figure 1c, and Section A for derivation and nondimensionalization of the original model). The spatial domain is scaled by the cell perimeter, L , so that the domain is $0 \leq x \leq 1$ (see Section A.2). Importantly, this model preserves the total mass of the GTPase, i.e.,

$$M := \int_0^1 [u(x, t) + v(x, t)] dx = \text{constant}. \quad (2)$$

A typical polar pattern throughout a thin, flat 2D cell shape (Figure 1c, left) is simplified to the corresponding pattern along the cell edge (Figure 1c, right). For example, a zone of active Rho corresponds, in this geometry, to a peak or plateau of u .

The model includes terms for Rho activation (basal, b and self-amplifying, γ) and inactivation (basal and GTPase dependent rate normalized to 1, F-actin dependent rate, s). The GTPase diffusion rates satisfy $D_u < D_v$ since active GTPase is bound to the plasma membrane, and diffuses slowly relative to the inactive form. The F-actin equation depicts assembly at a linear rate downstream of u (basal, p_0 and u -dependent, p_1) and first-order decay/disassembly. The parameter $\omega < 1$ governs the slow time-scale of actin dynamics. The rate of F-actin diffusion, D_F , is assumed to be very small or negligible. Importantly, the parameter, s , controls the strength of the negative feedback. When $s = 0$, F-actin does not affect Rho, the equations are decoupled, and the uv subsystem reduces to the wave-pinning (WP) polarity module. The model PDEs were simplified from [23] to polynomial (rather than Hill function) kinetic terms to facilitate mathematical analysis. See Appendix A for a more detailed description of the model derivation.

Parameter meanings and values are given in Table I. These values are chosen based on previous studies [41, 23] of similar models. The remaining parameter values are chosen based on the study by [27], who initially analyzed the model (1). Four parameters were varied in [27]. The negative feedback parameter, s , that represents the F-actin contribution to GTPase inactivation is the main parameter that shows coexisting regions of interesting solution types. The GTPase basal activation rate, b , together with s , is used to identify the key bifurcation that leads to the coexistence. The average GTPase density, M , was varied to show how high mass regimes lose polarity. Lastly, the domain length, L , introduced for mathematical convenience, is varied to demonstrate the effects of domain length on the types of observable patterns, which is equivalent to scaling the dimensionless diffusion parameters $D_i = D_{i,0}/(\delta_0 L^2)$ for $i \in \{u, v, F\}$, where $D_{i,0}$ and δ_0 represent

the dimensional diffusion rates and GTPase basal inactivation rate, respectively (see Section A). Following [27], we mainly focus on the parameter s and demonstrate how different domain lengths (or equivalently changes in dimensional diffusion rates and basal GTPase inactivation rate) can affect cell shapes and motility. Note that by choosing different kinetic rates as our time scale, δ_0 could be replaced by the basal GTPase activation rate, β_0 , or the self-amplifying GTPase activation rate, γ_0 .

2.2 Simulating cell shapes and motility

We use the cellular Potts model (CPM) to represent fluctuating cell shapes and cell motion. We chose the open-source multiscale software platform, Morpheus [49], as it has a built-in CPM simulator that enables solutions of PDEs such as (1) along a cell edge (implemented as a “membrane property”)¹. Those PDE solutions are linked to protrusion and retraction of that edge. Specifically, locations along the cell with high F-actin concentration are more likely to protrude outward and then the area constraint of the CPM promotes retraction. Details are explained further in Section B.

3 Results I: Analysis of model PDEs

We begin our analysis by describing the relevant bifurcation structures and solution types in this parameter regime. We set basic parameter values as in Table I, vary s and b to determine where in parameter space to expect interesting behavior, and then compute bifurcation diagrams in s , with various values of L , to identify different interactions between polarity and traveling waves.

3.1 Interesting parameter regimes

We start by understanding the bifurcation structure of the homogeneous steady states (HSS), i.e., solutions independent of space and time. To assess the stability of an HSS \mathbf{Q}^* , we use linear stability analysis, i.e., we investigate infinitesimal perturbations of the form

$$\mathbf{Q} = \mathbf{Q}^* + \epsilon \mathbf{Q}_1 + \mathcal{O}(\epsilon^2), \quad (3)$$

where $|\epsilon| \ll 1$ and \mathbf{Q}_1 is of $\mathcal{O}(1)$. The function \mathbf{Q}_1 is given by

$$\mathbf{Q}_1 = \zeta e^{\sigma t + iqx} + \text{c.c.}, \quad (4)$$

where $\text{Re}(\sigma)$ is the growth rate of the perturbation with wavenumber q , $\zeta = (u_1, v_1, F_1)$, and c.c. denotes the complex conjugate of the perturbation. Substituting the perturbation (3) into the model (1) and linearizing, leads to the eigenvalue problem

$$[\mathbf{J}(\mathbf{Q}^*) - q^2 \mathbb{D}] \zeta = \sigma \zeta, \quad (5)$$

where $\mathbf{J}(\mathbf{Q}^*)$ is the Jacobian of the reaction terms evaluated at \mathbf{Q}^* and $\mathbb{D} = \text{diag}(D_u, D_v, D_F)$ is the diagonal diffusion matrix. When analyzing the stability of \mathbf{Q}^* it is common to study the model (1) on the whole real line \mathbb{R} , as was done by [27]. To address this, we reintroduce a domain length L , i.e., we investigate (1) on the spatial domain $(0, L)$ without fixing the value of L . Therefore, the linear stability of \mathbf{Q}^* is determined if all $\text{Re}(\sigma) < 0$ for all $q \geq 0$. Bifurcations occur when there exists a wavenumber $q_* \geq 0$ such that $\text{Re}(\sigma(q_*)) = 0$ and all $\text{Re}(\sigma(q)) < 0$ for q near q_* .

The onsets of various bifurcations predicted by the model (1) are summarized in the two-parameter bifurcation diagram of Figure 2, where the basal GTPase rate of activation, b and the F-actin negative feedback rate, s are varied. The curves in these diagrams mark locations at which bifurcations leading to spatiotemporal patterns were detected in our previous analysis. The analysis is restricted to homogeneous steady states (HSSs), where curves of saddle-nodes (SN), finite wavenumber Hopfs (WBs, $\sigma = \pm i\omega$ for $q = q_* > 0$) suggesting the emergence of traveling and standing waves [30, 57], long wavelengths (LWs, $\sigma = 0$ for $q \rightarrow 0$), which have been shown to lead to the emergence of polar patterns after subsequent bifurcations [27], and, for completeness, homogeneous Hopf bifurcations (HBs, $\sigma = \pm i\omega$ for $q = 0$) are shown. (Note that in this regime, no Turing bifurcations are found ($\sigma = 0$ for $q = q_* > 0$)). Thus, this diagram provides a useful starting point for further analysis. It is important to note that this figure only shows where new

¹Technically, the PDEs are solved on the rim of a circle with the same area as the CPM cell, then mapped onto the CPM cell edge.

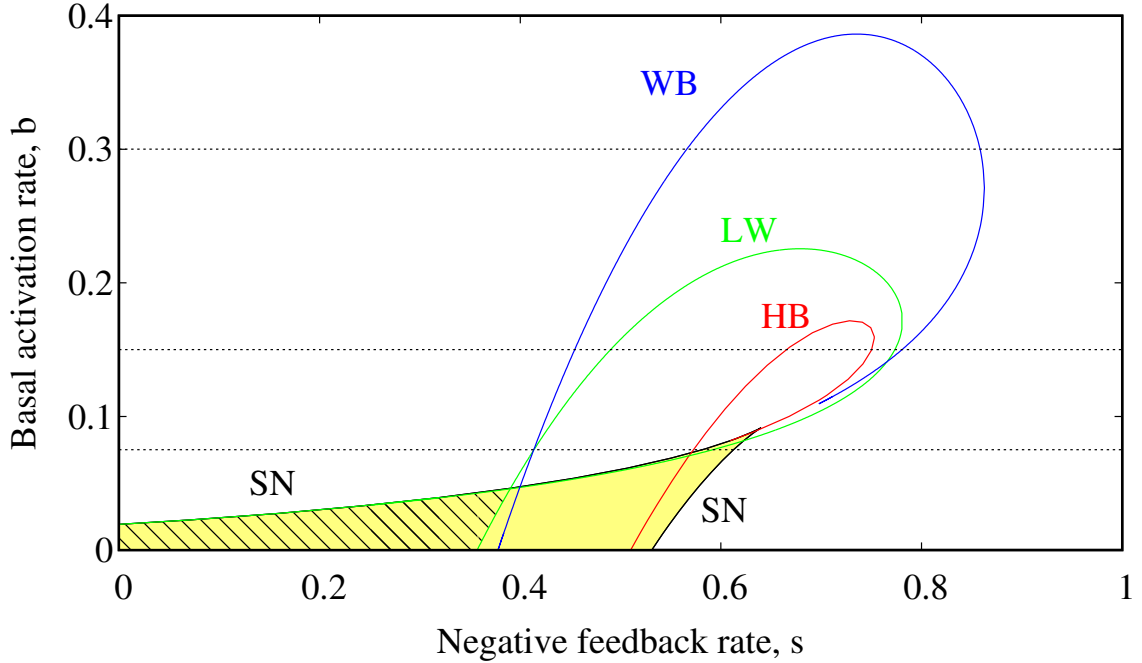


Figure 2: **Two-parameter bifurcation diagram of uniform steady states:** Parameters b, s were used to produce the two-parameter plane shown above. In [27], two-parameter continuation was applied to (1) to trace the onsets of bifurcations of the homogeneous steady states (HSSs). The bifurcations shown are finite wavenumber Hopfs (WB), long wavelengths (LW), homogeneous Hopfs (HB), and saddle-nodes (SN). The black-striped subset of the yellow region corresponds to the bistability region, where two HSSs out of three are stable. In the solely yellow-shaded region, there is at most one stable HSS. Note that the curves only indicate onsets of bifurcations, not regions of existence of a given pattern. The dashed lines denote b -value slices corresponding to values used in the parameter sweeps of the model (1) given in Figures 3 and 19.

spatiotemporal patterns emerge but not whether the solutions are stable or for which parameter values they exist. In particular, these curves do not represent boundaries where patterns exist only on one side. Instead, they denote parameter sets where spatiotemporal patterns emerge from the uniform steady states.

The curves shown in Figure 2 identify onsets where new types of spatiotemporal behaviors can emerge. Tuning the basal activation rate b (moving vertically on the diagram) or the negative feedback rate s (moving horizontally) can lead to identifying such onsets. Special points at the intersections of two curves (“codimension-2” bifurcations) denote parameter sets where both bifurcations occur simultaneously. Important in this work and previously identified in [27] is the codimension-2 bifurcation, where a long wavelength and finite wavenumber Hopf occur simultaneously. In [27], we showed that solutions representing polar and traveling wave states emerge from such a bifurcation, as described in more detail below.

Guided by the results of the numerical bifurcation analysis shown in Figure 2a, we identified an interesting region of the sb parameter space to explore. We then varied s and b in a 7×4 grid of values close to the codimension-2 point, and plotted the space-time solutions of the PDE equations (1) as kymographs. We used initial conditions of the form $a + b \cos(2\pi x/L)$ for each component, which favors the formation of solutions symmetric about $x = L/2$, i.e., stationary (polar) solutions. Results are shown in Figure 3. In each sub-panel, the spatial component (vertical axis) represents position along the cell edge, and time t along the positive horizontal axis. The color map displays the intensity of GTPase activity, $u(x, t)$. Uniform color depicts a cell edge with no “GTPase zone”. A horizontal band of color denotes a plateau of elevated GTPase (consistent with a polarized cell), and slanted stripes describe traveling waves (TW) that move clockwise or anti-clockwise around the cell perimeter.

In order to test for coexisting (bistable) behavior, we introduced random noise for a short time period to “scramble” the solution and permit a transition to another behavior that exists for the same parameter set. Several such transitions are evident in Figure 3, from polar to wave-like solutions ($s \approx 0.5$ and $0 \leq b \leq 0.15$), and from uniform to wave-like solutions ($0.7 \leq s \leq 0.9$ and

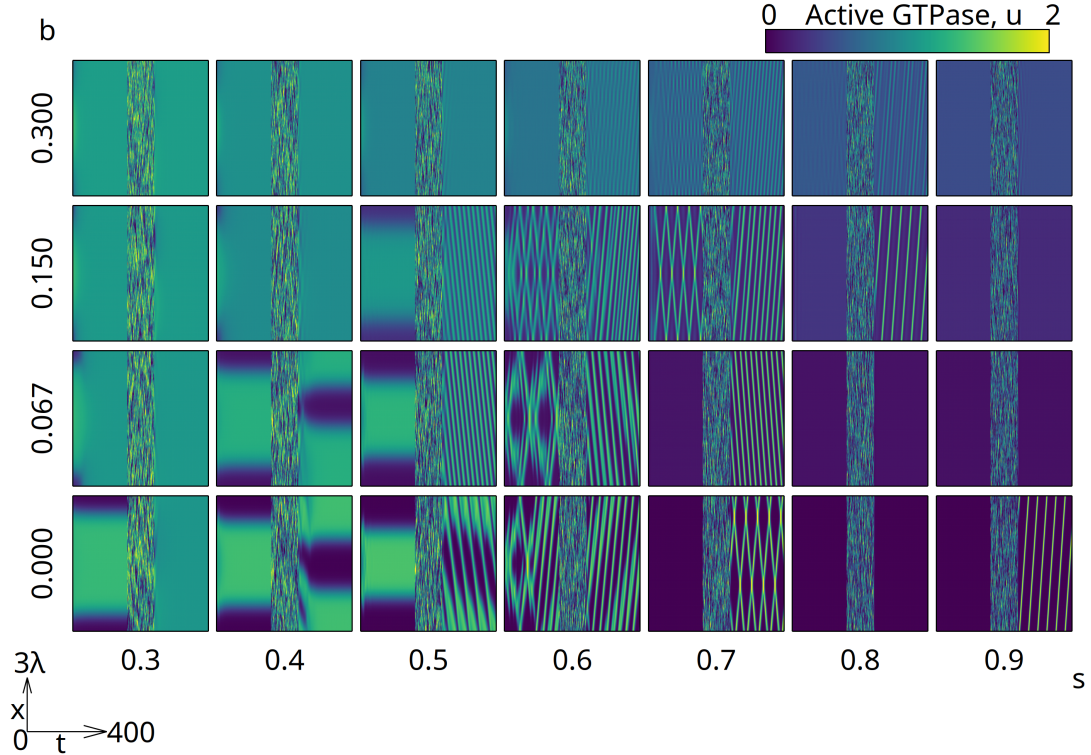


Figure 3: **Coexistence of polar and ruffling states in time-dependent simulations.** Same idea as in Figure 2 but showing the full PDE solutions as the parameters s, b are scanned with $L = 3\lambda \approx 9.28$, where λ is the wavelength that induces the finite wavenumber Hopf instability of the upper HSS. Solutions are shown as space-time kymographs of the active GTPase, $u(x, t)$ as a heat map, for several values of the basal GTPase activation rate, b (0, 0.067, 0.15, 0.3 on vertical axis) and various values of the negative feedback parameter s (horizontal axis, $0.3 \leq s \leq 0.9$). The system is initiated with $u(x, 0) = 0.75 - 0.5 \cos(2\pi x/L)$, $v(x, 0) = 1.25 - 0.1 \cos(2\pi x/L)$, and $F(x, t) = 3.5 - 2 \cos(2\pi x/L)$, and simulated to $t = 400$. For $160 < t < 240$, white noise is added to the du/dt equation and subtracted from the dv/dt equation (to avoid changing the total mass M). The noise results in several transitions between coexisting states such as polar, TWs, uniform steady states, and more complex time-periodic dynamics. If s is too small or too large, only the uniform state exists. Profiles of u, v, F at $t = 400$ corresponding to these kymographs are shown in Figure 4. Other parameter values as in Table I.

$0 \leq b \leq 0.15$). Note that initially the solutions are symmetric, e.g. polar and uniform patterns, because of the choice of initial condition. We also see cases where waves move in one direction, or in opposite directions. We found that if s is too high or too small, no wave-type solutions were possible. Figure 19 is another parameter sweep with $L = 2\lambda$, showing that fewer types of transient dynamics are possible with smaller domain lengths but the overall ‘‘long run’’ dynamics are similar. These full PDE solutions confirm the predictions of the bifurcation study.

We further plotted the profiles of all three variables, u, v, F at the final time point ($t = 400$) to demonstrate the relationship of the model components. As shown in Figure 4, the inactive GTPase is nearly spatially uniform, while the dominant patterns reside in u, F . (This follows from the fact that v diffuses fastest, so that it rapidly redistributes along the domain.) Furthermore, we note that for the propagating solutions, such as the traveling waves, the peak of F trails after the peak of u (see the arrows in Figure 4 that denote the direction of propagation). This behavior arises from the diffusion coefficients, that is, $D_F < D_u$.

3.2 Coexistence and transitions between regimes

From the simulations of the model (1) in Figure 3, we see that certain parameter settings admit more than one possible behavior, that is, there is coexistence of distinct solution types. Transitions between those types were elicited by noise, without changing parameter values. We wish to understand the regimes of coexistence by considering the one-parameter bifurcation diagrams of the PDEs.

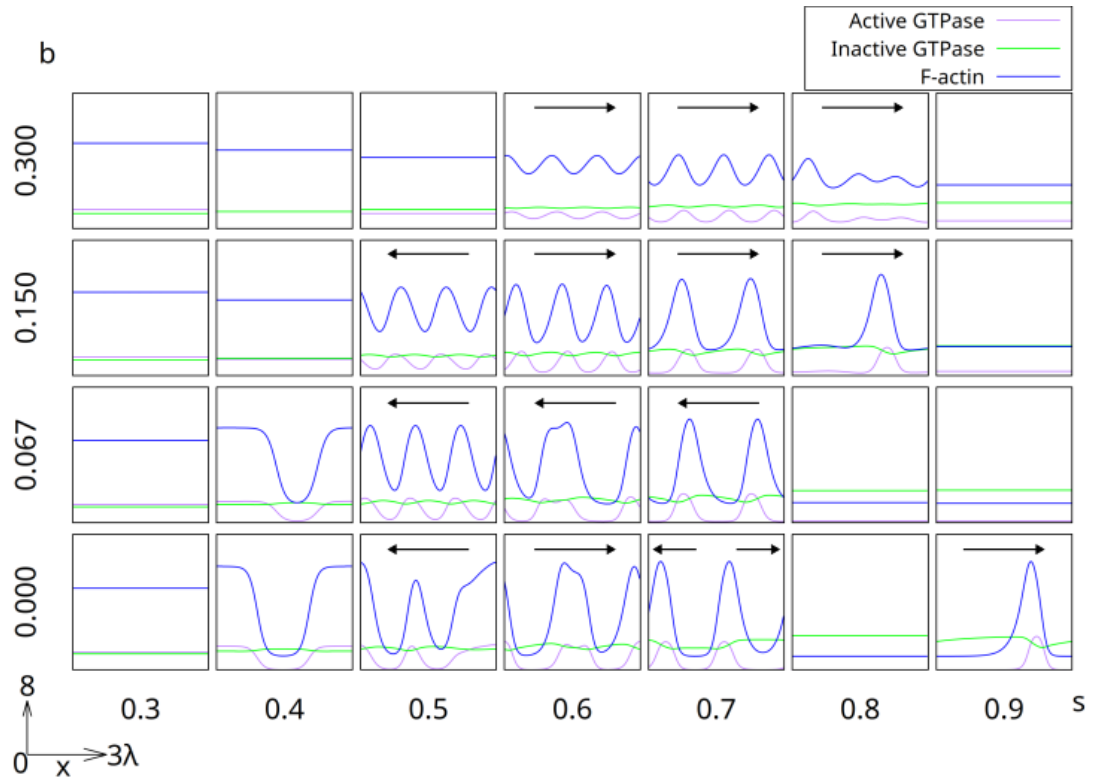


Figure 4: **Final solution profiles from Figure 3.** Line plots showing the u, v, F profiles at $t = 400$ for the simulations in Figure 3. We see uniform states for small and large values of s , traveling waves of 3, 2, or 1 wavelengths for intermediate values of s , and polar patterns for $s = 0.4$ and small b . The inactive GTPase (green) is nearly uniform due to its relatively high rate of diffusion. The arrows indicate the direction of propagation. When $b = 0$ and $s = 0.7$, counter-propagating waves are observed and the arrows demonstrate the direction each wave travels.

From here on, we focus primarily on the effect of the negative feedback from F-actin, governed by the parameter s . Single-parameter bifurcation plots for two distinct domain sizes (cell perimeters, L) are shown in Figures 5 and 6. These diagrams show traveling wave and polar solutions with different wavelengths and thus provide detail on where, in parameter space, these solution types exist and, in particular, coexist. We set the GTPase basal activation rate to a constant value $b = 0.067$, corresponding to a horizontal cut in Figure 2 and the horizontal row with $b = 0.067$ in Figure 3 and Figure 4. Here, a codimension-2 long wavelength/finite wavenumber Hopf bifurcation is observed as s is varied (see [27] for more details). The wavelength of the finite wavenumber Hopf bifurcation is numerically determined to be $\lambda \approx 3.09$.

We choose the cell perimeter $L = 3\lambda$ as our main regime (see Figure 5 for the bifurcation diagram). Here, the emerging nonuniform solutions are at or near the codimension-2 long wavelength/finite wavenumber Hopf, multi-peak traveling waves (“ruffling”) coexist with polarization, and there is a broad parameter regime where polar patterns exist without traveling waves. This figure summarizes transitions in behavior as we move along the horizontal direction in Figure 2 (at fixed $b = 0.067$, a given cell size, fixed total amount of GTPase, and all other parameters held constant). That is, we are only tuning the F-actin negative feedback s .

The bifurcation diagram in Figure 5 informs us of several trends: (1) Varying s leads to transitions between stable states: from a uniform state with no pattern (low s , white region), to a polar state (yellow shaded region), to a wave-like “ruffling” state (purple), and back to uniform. These transitions are depicted by the endpoints of solid curves in each case. It is important to note that other solution types exist in this regime, including bipolar and tripolar patterns, and traveling waves with 1 and 2 peaks (see [27] and Figure 17 for more details). The bipolar and tripolar patterns are all unstable (a characteristic property of mass-conserved systems [56]) and so we focus on unipolar patterns. Also, other solution types that exhibit similar polar and ruffling cell states may exist in this regime. (2) There is a substantial range of values of s for which both polar and ruffling states coexist and are stable (overlap of yellow and purple regions, shown as orange region). (3) Other states (dashed lines) exist in various parameter regimes, but are unstable, and would not be observed biologically in the long term (but could lead to transient behavior). (4) Polar cell states exist for lower negative feedback strengths s whereas traveling waves exist for higher s values. (5) The structure of the solutions and the bifurcation points (at which stability changes occur or new solutions emerge) can be classified in terms of known dynamical systems transitions, shedding light on their “generic” (model independent) properties. For example, mass conservation is necessary for the polar patterns to exist for broad parameter regimes. In particular, mass conservation allows for such patterns to form without coexistence of HSSs and causes them to not propagate in space [53].

The bifurcation diagram with cell perimeter $L = 5$ (see Figure 6) shows different transitions between polar and traveling wave states (see [25] for more details). (Note that a similar structure is also observed with $L = 3\lambda/2$ but the stability region of the polar patterns is much smaller.) Here, there is no coexistence between these states, but there is a continuous transition between polarization and cell turning. In particular, the stable traveling waves emerge from a so-called parity-breaking bifurcation of the stable polar solutions, where separate branches of left and rightward moving traveling waves emerge with the same wavelength. This structure suggests a possible mechanism for transitioning between cell turning and polarity by slowly varying s between the two regimes of stability. Such an investigation is performed in Section 4.6.

In Section C, we show a more complete bifurcation diagram for the cell perimeter $L = 3\lambda$ with traveling waves and polar patterns with 1, 2, and 3 peaks and the corresponding structure when $L = 2\lambda$.

4 Results II: Cell shapes and motility

As mentioned, we will now connect the PDE solutions to a moving cell framework via CPM simulations that depict cell shapes and migration. We set basic parameters at the same default values as in our bifurcation plots (see Table I), and vary the parameter s and cell perimeter L , and fix $b = 0.067$. For each case, we pick values of s and L , and construct initial conditions close to solutions on specific branches of the bifurcation diagrams (Figures 5, 6 and 18) and display PDE solutions as kymographs of $u(x, t)$. Therefore, in all simulations there is some initial transients as the system is not exactly at a steady state. In some cases, the same color scheme also shows $u(x, t_i)$, at various times t_i , along the edge of the 2D CPM cell. We also show a time sequence of cell shapes and locations to demonstrate dynamics and motion of those cells. The parameter values and initial conditions used in the simulation are described in Section D. Note that results

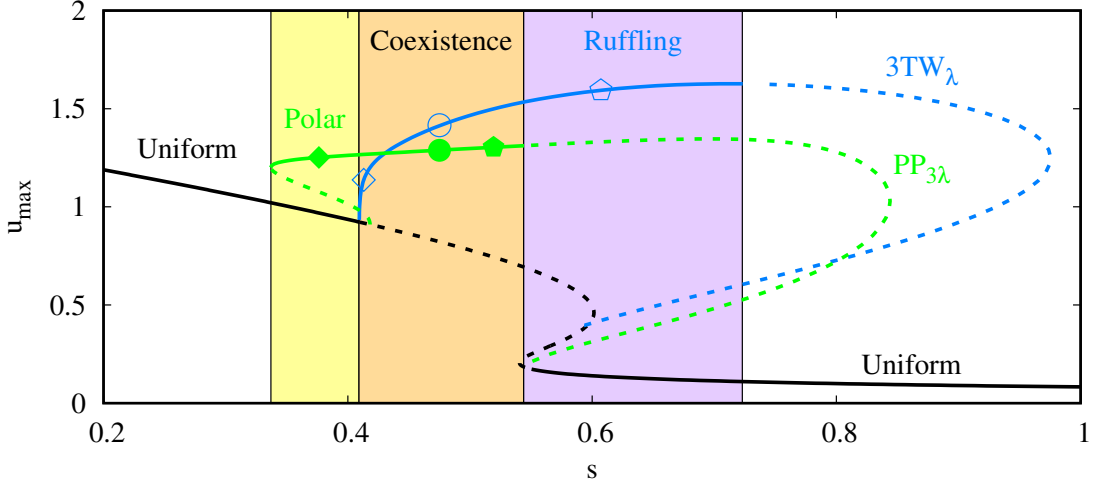


Figure 5: **Coexistence of polar and ruffling states:** Single parameter bifurcation diagram with respect to the negative feedback parameter, s , for $b = 0.067$ and $L = 3\lambda$, where $\lambda \approx 3.09$ is the wavelength that leads to the instability of the upper HSS. The solutions are projected onto the maximum value of the active GTPase, u_{\max} . Solid lines denote linearly stable solutions (i.e., observable in the long run) and dashed lines denote unstable solutions. Uniform HSSs (solid black curves) represent an unpolarized “resting cells” with spatially uniform GTPase activity around its perimeter. Polarized states ($PP_{3\lambda}$) are stable along the green solid curve. Waves with 3 peaks ($3TW_{\lambda}$, “ruffling”) are stable along the solid blue curve. As s increases, transitions in behavior are predicted: from uniform to polar, from polar to ruffling, and from ruffling to low uniform stable state. However, not all possible solution types are illustrated. For example, traveling waves with 1 and 2 peaks and bipolar and tripolar patterns also exist in this regime (see [27] and Figure 17 for more details). In the orange shaded region, both polar and ruffling states coexist, so transitions between them can take place. Typical solutions are shown in the $b = 0.067$ row of Figure 3. The shapes and motility behavior of cells corresponding to points along these curves are shown in Figures 7 to 9.

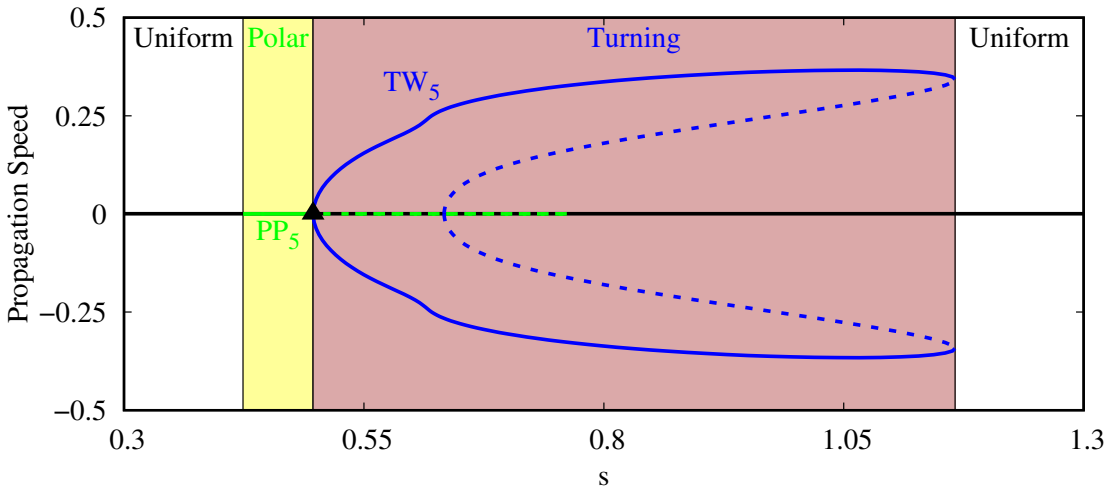


Figure 6: **Transition between polarization and turning:** Single parameter bifurcation diagram as in Figure 5 but with $L = 5$ and projected onto the propagation speed of the solution. In this diagram the traveling wave solutions (TW_5) have 1 peak and represent cell turning. Here, we see that there is no coexistence between static polar patterns (PP_5) and traveling waves. Instead, the polar patterns lose stability at a parity-breaking bifurcation (at $s \approx 0.497$, black triangle) caused by the loss of reflective symmetry (i.e., loss of the invariant $x \rightarrow -x$), which leads to the emergence of stable traveling waves. Note that as in Figure 5, not all possible solutions are shown. Simulations investigating the transition from polar to cell turning as s is varied are shown in Figures 12 to 14.

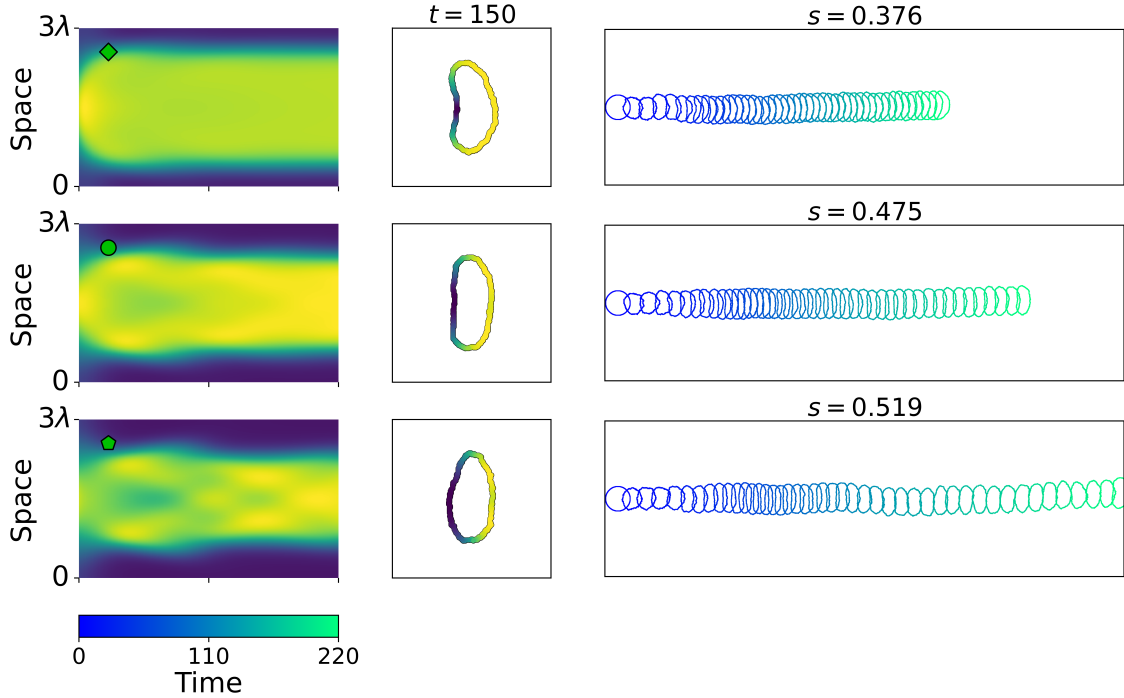


Figure 7: **Shapes and trajectories of polar cells corresponding to points on the polar branch in Figure 5:** Three simulations of PDE solutions in kymographs (left), resulting cell shapes (center) and motion (right) simulated in Morpheus [49]. The cell locations over time are shown (right) with heatmap for $0 \leq t \leq 220$. The results correspond to the green symbols on the (polar) branch in Figure 5, for $s = 0.376, 0.475, 0.519$, i.e., the cell perimeter $L = 3\lambda$. Some transients are shown in each case. Note that as s increases, the width of the Rho zone shrinks, making Rho more highly concentrated at the front. This results in increased F (not shown) and greater cell speed. It also accounts for a transition from “canoe” to “D” keratocyte-like cell shapes after some transients. Initial conditions provided in (11), and other parameter values as in Table I. Domain size is $L = 3\lambda$, where λ is the wave-length of the traveling wave solutions in Figure 5. Morpheus file: Polar Files.

in this section can be reproduced by running Morpheus with the xml file linked to a given figure.

4.1 Polar cells display directed motion

We first consider the dynamics of cells, corresponding to points marked by green shapes along the green “polar” branch in Figure 5. Results are shown in Figure 7 for values of $s = 0.376, 0.475, 0.519$ (green diamond, circle, and pentagon, respectively, in Figure 5). The initial conditions lead to some transients while the distribution of components along the cell edge settles into its steady polar profile. During these transients, the cell shape oscillates but directed cell motion persists.

The fastest, and most polarized cell is found at $s = 0.519$. This cell has the narrowest, tallest plateau of u , seen from the width of the yellow band in the kymographs. This value of s leads to the most focused “cell front”, where the active GTPase and F-actin are densest. We can understand the cell speed from the fact that protrusion is assumed to be proportional to F , and F tends to a value proportional to u in the model. Hence, a higher GTPase level at the front implies a higher F-actin density and stronger protrusion force.

The steady state shape of the cell also depends on s . This is demonstrated in the central column of Figure 7 where both steady state cell outlines and values of u along the edge are shown. On the whole, these simulations bear a significant resemblance to the polarized motion of keratocytes.

4.2 “Ruffling” cells do not migrate

We initiated cells with the same set of basic parameters (other than s), but with a distinct initial distribution of components along their edge, to demonstrate the behavior close to the “ruffling” branch in Figure 5. In particular, we used initial conditions with three peaks that have an initial asymmetry in the model components so that propagation is favored. Results are shown in Figure 8.

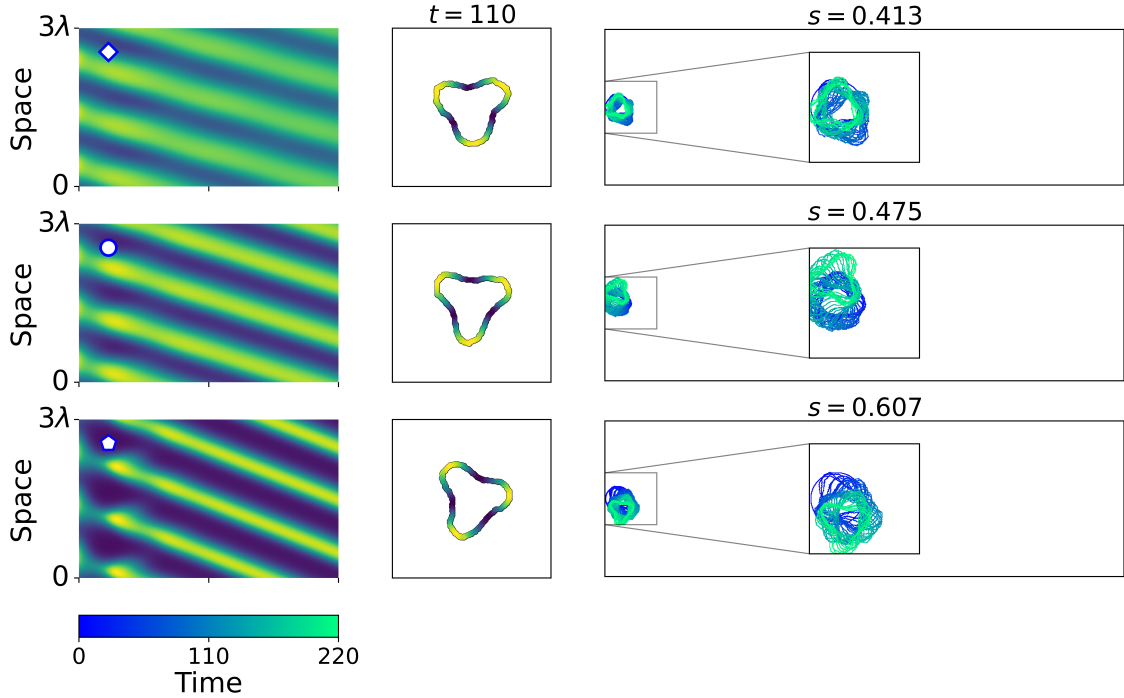


Figure 8: **A “ruffling” (3TW) cell hardly moves:** As in Figure 7, but for the traveling wave branch in Figure 5 with $s = 0.413, 0.475, 0.607$. Parameter values corresponds to shapes along the blue branch in Figure 5. The insets of the right panels show a zoomed-in view of the various cell shapes. Note that the cells have three competing protrusions, and have no directed migration. This figure was produced with the same parameter values as in Figure 7 (Table I), but with different values of s and different initial conditions (see (12)). Morpheus files: 3TW Files.

After some transients, the PDE solutions form traveling waves with three peaks. Correspondingly, each of the simulated cells settles into a shape with three protrusions circulating around the cell perimeter. As a result, there is no unique “front”. Directed migration is lost entirely, and the cells appear to rotate in situ. The rotation speed increases with larger s values, due to higher propagation speed of the traveling wave in the underlying PDE system (1). Note that the middle rows of Figures 7 and 8 have identical parameter values, and differ only in initial conditions. This verifies the stable coexistence of polar and ruffling cell states.

The waves of these ruffling model cells are reminiscent of waves of edge protrusion seen in the Sheetz lab [20] in mouse embryonic fibroblasts (MEFs) (see their SI movies 5, 7, 14), and was later quantified in MEFs, fly wing disk cells, and mouse T cells. (Figure 2 in [17].) Typical edge protrusion speeds observed there were 0.5-5 $\mu\text{m}/\text{min}$.

4.3 Destabilized polar cells have dynamic shapes

For the given parameters (see Table I) and cell perimeter $L = 3\lambda$, polarization destabilizes at $s \approx 0.54$. From [27], we know that the instability is a Hopf bifurcation, suggesting the emergence of oscillations around the polar distribution. In [26], a simulation governed by this instability was investigated in the context of real cells hitting a wall. In particular, Hughes *et al* demonstrated that the underlying instability captured the initial transition from directed to disordered motion post collision. Here, we show how cell shape and migration are affected by this instability in the context of CPM simulations. Figure 9 shows the resulting simulation. We used the same initial conditions as in Figure 7, but with $s = 0.55$, which is just past the onset of instability of the polar patterns.

After some initial transients, the distribution of GTPase settles into a time-periodic oscillation around a polar distribution. The distribution of the GTPase still maintains a region of high activity that does not translate along the edge of the cell. This causes the cell to maintain directed cell motion. However, the shape of the cell oscillates between ‘D’-like, oval, and ‘kidney’ shapes. The distribution of the GTPase around the kidney shape shows that the peak of GTPase is not always in the direction of motion. Instead, at these instances, there are two competing “fronts” that coordinate to maintain directed motion. The simulation in Figure 9 shows that at this instability,

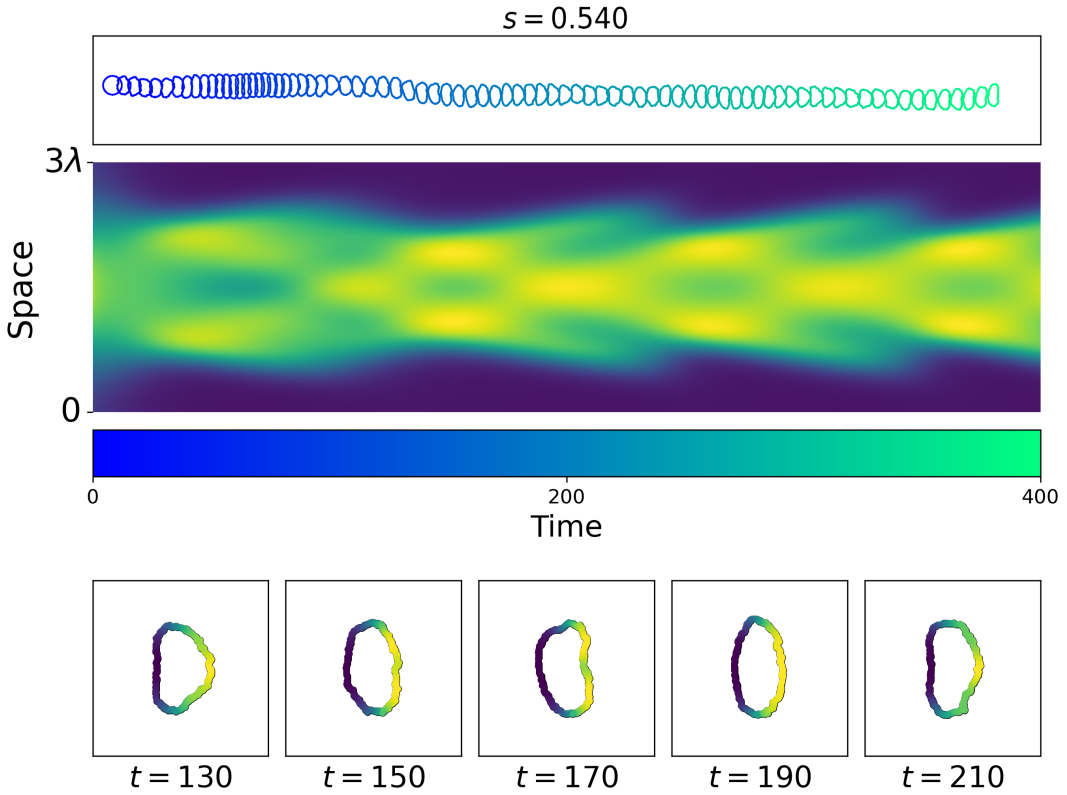


Figure 9: **Destabilized polar cells:** The shapes and motion of a cell that is initiated with the same conditions as Figure 7, but with $s = 0.54$, i.e., after the instability of polar patterns. Here, the cell locations over time are shown at the top, the PDE solution as a kymograph in the middle, and active GTPase concentration along the cell edge at the bottom. Note the oscillations in cell shape and speed. Produced with Wobby_s_0.600.xml.

directed cell motion persists. Therefore, to fully transition to disordered motion, additional instabilities, stochastic effects, higher dimensionality, or more complex signaling networks are needed (as predicted in [26]).

4.4 Exotic trajectories and coexisting modes in smaller cells

From the simulations in Figures 3 and 19, we see that time-periodic patterns can form, resembling counter-propagating peaks. In the following simulations we use $L = 2\lambda$, $s \in \{0.6, 0.8\}$ and retain all other parameters. We choose $L = 2\lambda$ because at $L = 3\lambda$, the resulting solutions have additional peaks that interfere with the counter-propagating peaks. The bifurcation diagram for cells of this size is shown in Figure 18. However, the time-periodic solutions that are observed are not presented in that figure. Note that the distinct cell size produces distinct ranges of stability of polar and wave-like solutions. Here, we explore the results for counter-propagating waves as well as single traveling waves.

4.4.1 Counter-moving protrusions

We ran simulations with cells initialized with polar initial conditions but with $s = 0.6$, which is after the instability onset of polar patterns ($PP_{2\lambda}$). As shown in Figure 10, the polarized distribution rapidly destabilized, first into a few standing oscillations (left portion of kymograph), and then into a pair of traveling waves (TW) moving in opposite directions. These counter-moving traveling waves result in two protrusions circulating around the cell's edge.

While the two protrusions are close to one another, they coordinate and determine an “effective front” propelling the cell in a compromise direction. As the waves reach the cell “rear”, the cell reverses its direction of motion. As seen in Figure 10, this sets up a back and forth migration pattern. The shapes of the cell also fluctuate periodically, with two protrusions merging and splitting along the cell edge. This indefinite cycle of shapes and motion stems from our simplified cell-edge domain, and would not be likely to occur in real cells, where waves are prevented from

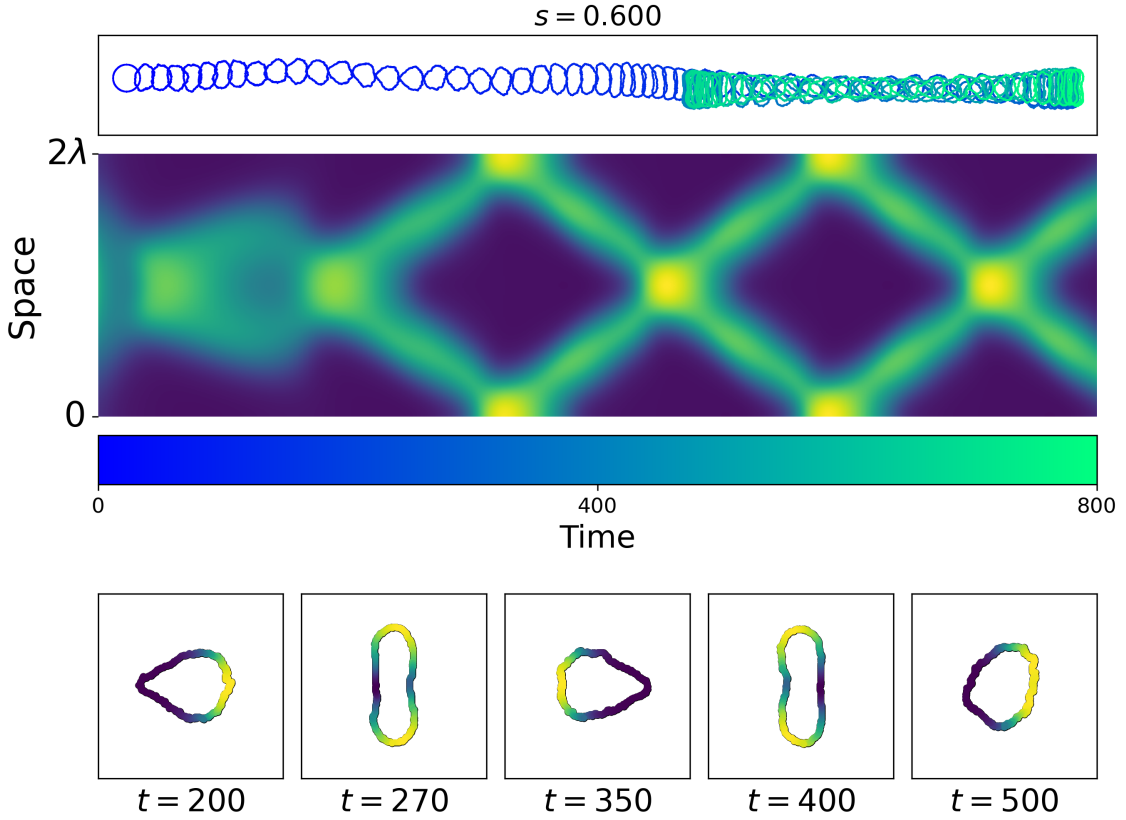


Figure 10: **Coexisting motility modes:** A simulation as in Figure 9 but in a smaller cell (with perimeter $L = 2\lambda$, where λ is the critical wavelength of TW instability) and with $s = 0.6$. The cell, initiated in a polar state, starts to oscillate. Two counter-propagating peaks then get established, which oscillate back and forth. The cell moves forward and back as the waves propagate around its rim. Initial conditions given in (13). The cell continues in its wobbly periodically shifting state. Morpheus file: CW_s_0.600.xml.

reaching the cell “rear”.

4.4.2 Cells with one or two protrusions

For cells of size $L = 2\lambda$, there are regimes where one or two-peak traveling waves can coexist. To visualize transitions between these states, we initiated simulations in the same way as in Figure 10, and added noise after some time, to see transitions. Results, shown in Figure 11 demonstrate the distinct cell behavior when one or a pair of (countermoving) TWs are present.

In both cases, counter-moving TWs became established early in the simulation. Following application of noise (red band on kymograph), roughly 9 out of 10 cases reverted to the same counter-propagating peaks. In a few cases, including top panel of Figure 11, only one peak persisted after the noise.

When a single-peak TW remains, the cell has a unique “front edge” that circulates around its edge. Consequently, the cell trajectory is circular, with a polarized skewed cell shape. This contrasts with the 2TW case, where the cell moves back and forth, as previously found. In the latter case, the noise changes the axis of migration, but not the overall behavior. These results confirm the coexistence of dynamical states such as single peak TWs and time-periodic solutions in the model.

Single and multiple traveling waves have been observed in real cells. For example, [33] found that mouse embryonic fibroblasts (MEFs) and PtK1 epithelial (kidney) cells display modulated traveling waves moving bidirectionally around the cell edge (e.g., [33] Fig 10). For PtK1 cells, the authors found noisy counter-propagating traveling waves with wave-speed of $\approx 6\mu\text{m}/\text{min}$.

4.5 Static resting cells at low and high values of s

We explored several other settings with similar parameters but for large and small values of s that are outside of the pattern-forming range (results not shown). For low and high values of s ,

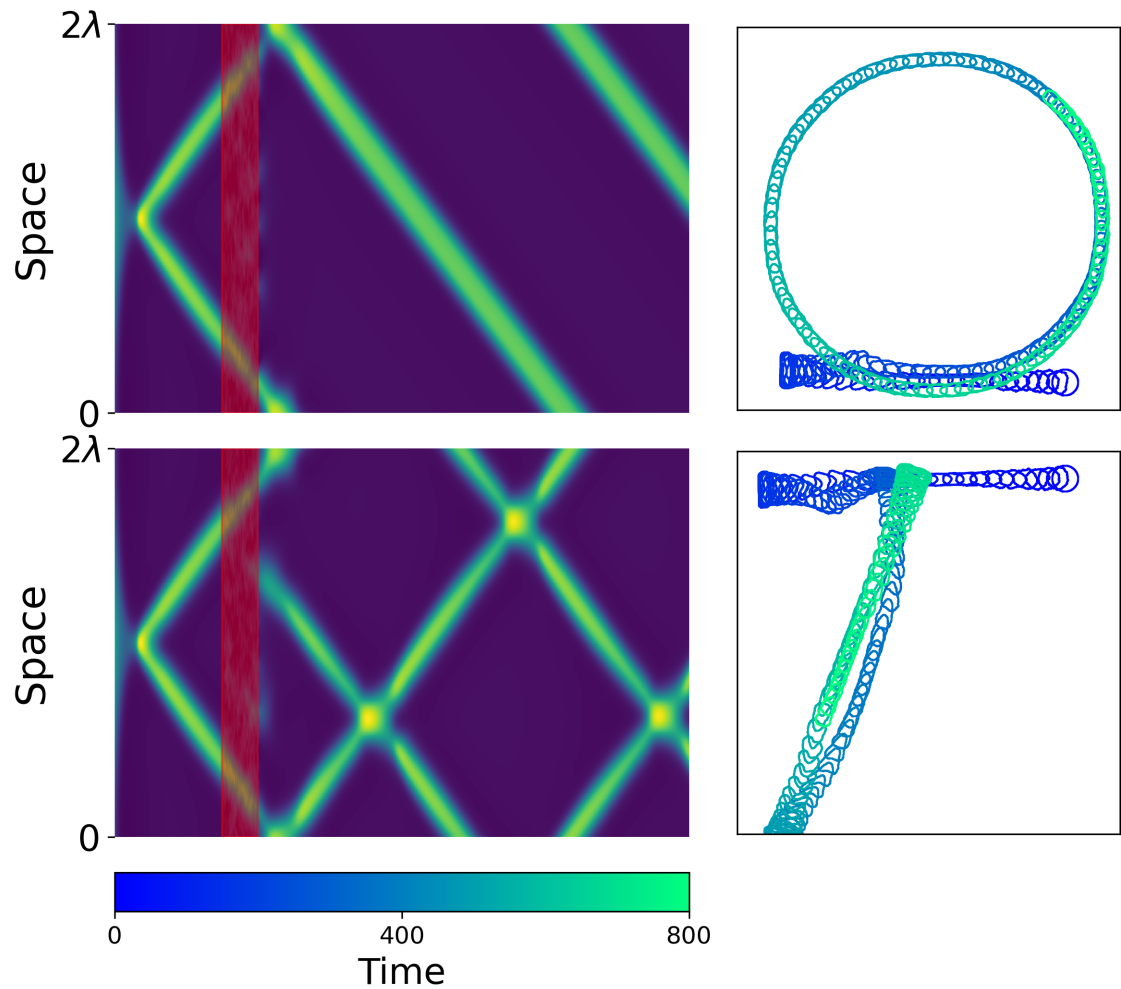


Figure 11: **Exotic trajectories:** As in Figure 10, but for $s = 0.8$ and with noise at $150 < t < 200$ (red stripe). The resulting single or double counter-propagating waves lead to small circular trajectories (top) or reversal of cell motion (bottom). Initial conditions and other parameters as in Figure 10. Morpheus file: CW_s_0.8_noise.xml.

e.g., $s = 0.2$ and $s = 1.3$, respectively, all nonuniform patterns shown cease to exist, and only a uniform spatial distribution of u, v, F is stable. In these cases, an initially polar cell rapidly loses polarity and stalls. The distance that an initially polarized cell can move in that case depends on the timescale of the u, v, F components relative to the persistence time assumed in the cell simulations.

Results so far are for cell behaviors at specific constant parameter sets. We next investigated transitions in cell behavior that accompany time-dependent values of the negative feedback rate, $s(t)$.

4.6 Transitions for time-dependent F-actin negative feedback.

Motivated by Figure 6, where stable traveling waves emerge from stable polar patterns, we provide simulations with a time varying F-actin dependent inactivation rate, $s(t)$. In particular, we vary s so that we cross this parity-breaking bifurcation and see transitions between polar cells and cells with a single traveling wave along its perimeter. The domain length is set to $L = 5$ in these simulations to match that of Figure 6. Results are shown in Figures 12 to 14.

We first consider a linear time-dependent increasing ramp for $s(t)$ over the range $0.475 \leq s \leq 0.6$. This ramp sweeps across the polar and TW regimes of the model. As shown in Figure 12 (left to right), the cell is initially polar, and moves directionally rightwards. As s increases, the width of the plateau region of high GTPase decreases, and is eventually replaced by a single-copy traveling wave. As a result, over the final 200 time units, the cell traverses a circular path showing cell turning (see the inset of Figure 12 showing one revolution of the circular path). Notably these transitions are relatively sharp, as predicted by our bifurcation analysis.

A similar transition, but for a decreasing ramp of $s(t)$ over the same range $0.6 \geq s \geq 0.475$ is shown in Figure 13. As s decreases, the propagation speed of the traveling wave decreases to zero, and then a polar distribution emerges. Afterwards, the cell moves along an oblique path to the bottom-right of the domain.

Finally, we allow $s(t)$ to vary randomly within the range $0.475 \leq s \leq 0.6$. (This was implemented as a kind of random walk of the parameter s within this range, with reflective boundaries at the interval endpoints.) As shown in Figure 14, the resulting kymographs demonstrate transitions in behavior. The cell shapes and trajectory (left to right) produce a mixture of the motility modes discussed above, and the cell moves randomly in its domain. Interestingly, for $100 \leq t \leq 400$, we also see counter-moving peaks as in Figures 10 and 11. This suggests that s is varying too fast and the polar patterns destabilize into these periodic solutions as seen in the aforementioned figures.

4.7 Connection to real cells

The minimal model for actin regulation (1), together with the basic CPM simulation would not be expected to capture the complexity of real cells. Nevertheless, several examples described have aspects that resemble motion observed in real cells. This is true of the polarized motion of keratocytes, shown in the experimental cell contour data from [45]. Two samples of this type, for polar and turning keratocytes are reproduced in Figure 15a,b.

However, cells of the social amoeba *Dictyostelium discoideum* display less regular migration, with alternations between dominance of one or another pseudopod [28, 42, 26]. This gives rise to the kind of dynamics shown in Figure 15c. We asked whether our prototypical model could capture any aspects of such behavior given the addition of spatially-dependent periodic noise that interferes with one or the other waves moving around the cell.

To probe this possibility, we initiated a cell with the same conditions as in Figure 11, but with noise at one or the opposite cell edge with periodic intensity. (See Appendix for details.) Results of this trial are shown in Figure 16. The kymograph demonstrates that protrusions (bright stripes of activity of u) alternate moving right versus left in an irregular manner. This affects both the cell shapes and cell trajectory. In this basic model variant, we cannot claim to adequately account for the *Dictyostelium* motion. However, we do see that pseudopod dominance and cell trajectories have some features in common with Figure 15c. For more detailed pseudopod-competition model of *Dictyostelium*, see [42].

5 Discussion

Our main goal in this paper was to leverage recent analysis of a prototypical model for F-actin regulation to reveal its implications for cell shapes and migration. The existing theory consisted of

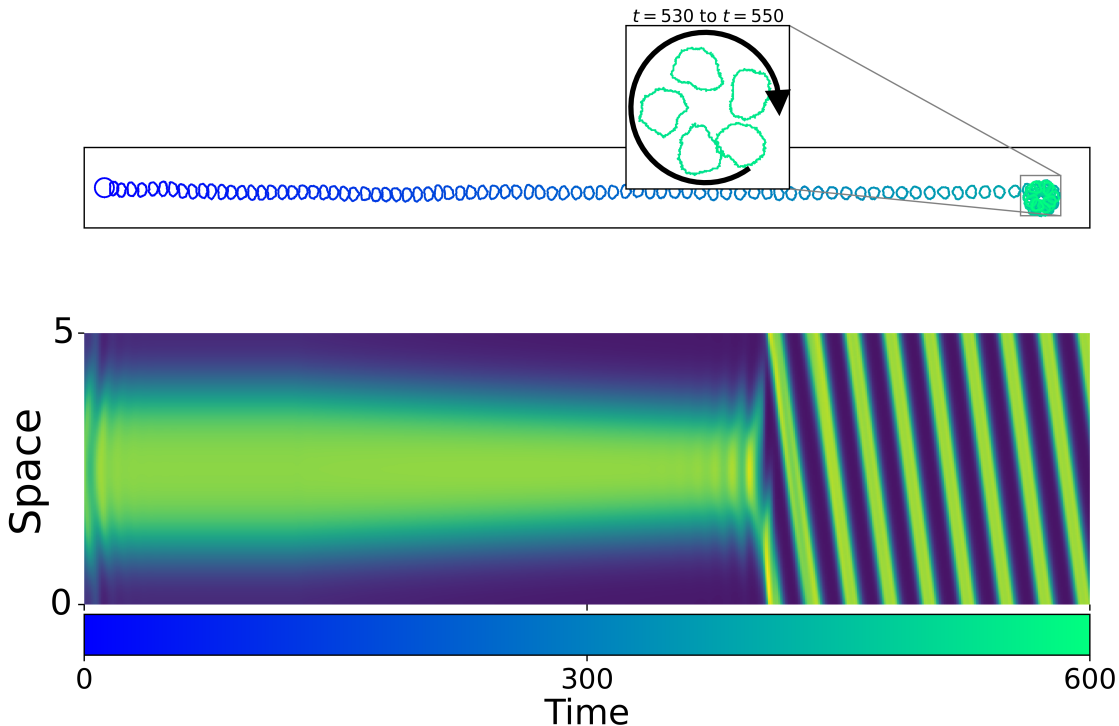


Figure 12: **Transition from directed cell motion to cell turning:** The simulation starts with a polar initial state (13), and $s = 0.475$. At time $t = 125$, the value of s grows linearly according to (15), attaining $s = 0.6$ at $t = 375$. This causes the polar pattern to become a single traveling wave. Kymograph of u (bottom) and cell shapes and trajectory (top) are shown. The inset shows one full cycle of the cell shapes along the circular path induced by the single-peak traveling wave. Produced with Morpheus file POLAR2TW.xml

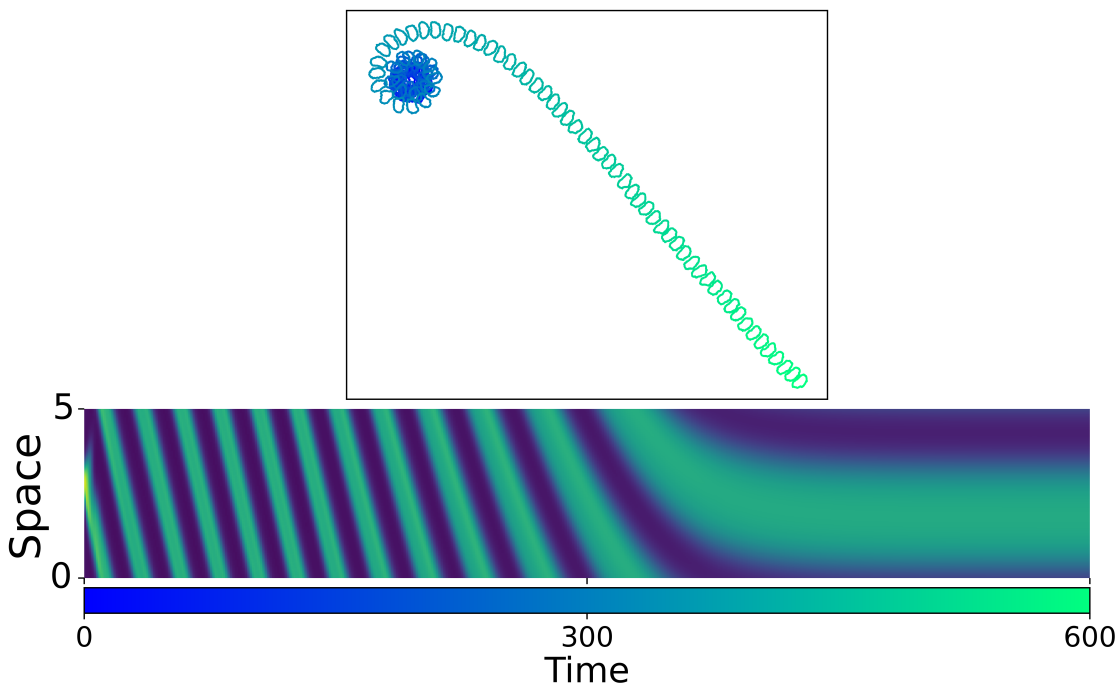


Figure 13: **Transition from cell turning to directed cell motion:** As in Figure 12, but with $s_0 = 0.6$ (for $0 \leq t \leq 125$) and $s_f = 0.475$ (for $t \geq 375$). Initial conditions given by (16) form a traveling wave that turns into a polar solution as s decreases. The cell starts by traversing a circular path as in the end of the simulation shown in Figure 12 (blue part of image, top), and later moves in a polarized manner towards the bottom-right. Produced with Morpheus file TW2POLAR.xml.

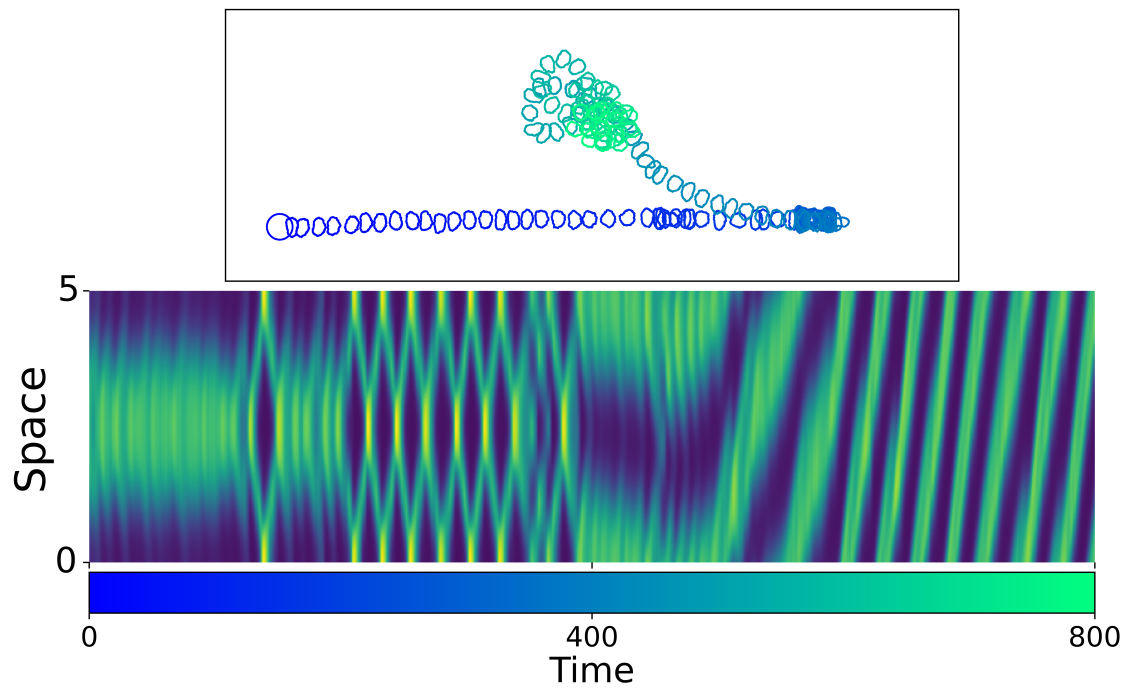


Figure 14: **Randomly changing $s(t)$:** As in previous figures, but with $s(t)$ constantly evolving randomly within the interval $0.475 \leq s \leq 0.6$ based on Weiner process (essentially, Brownian motion with reflective boundaries at $s = 0.475$ and $s = 0.6$.) We see random switching between polar, counter-propagating peaks, and traveling waves. Each run is unique, but all start with the polar configuration. Produced with Morpheus file Random_motion.xml.

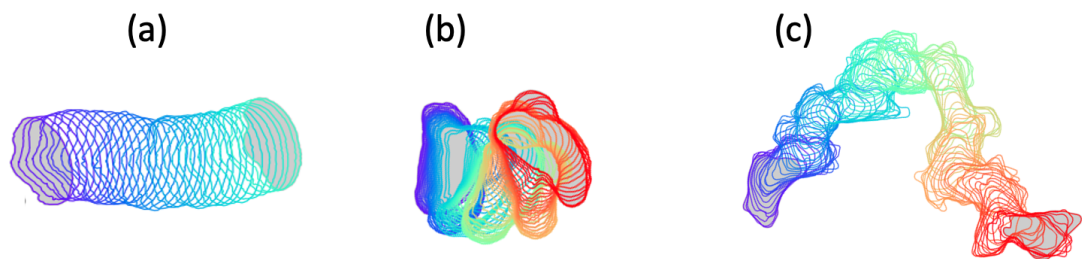


Figure 15: Distinct modes of cell motility in real cells from [45]. Cell contours (time increases from purple to light green and then red) for (a,b) polar and turning keratocytes and (c) amoeboid motion of a *Dictyostelium discoideum* cell. Adapted from Figs 6 and 11 in [45], published under the CC BY 4.0 License, in PLOS One.

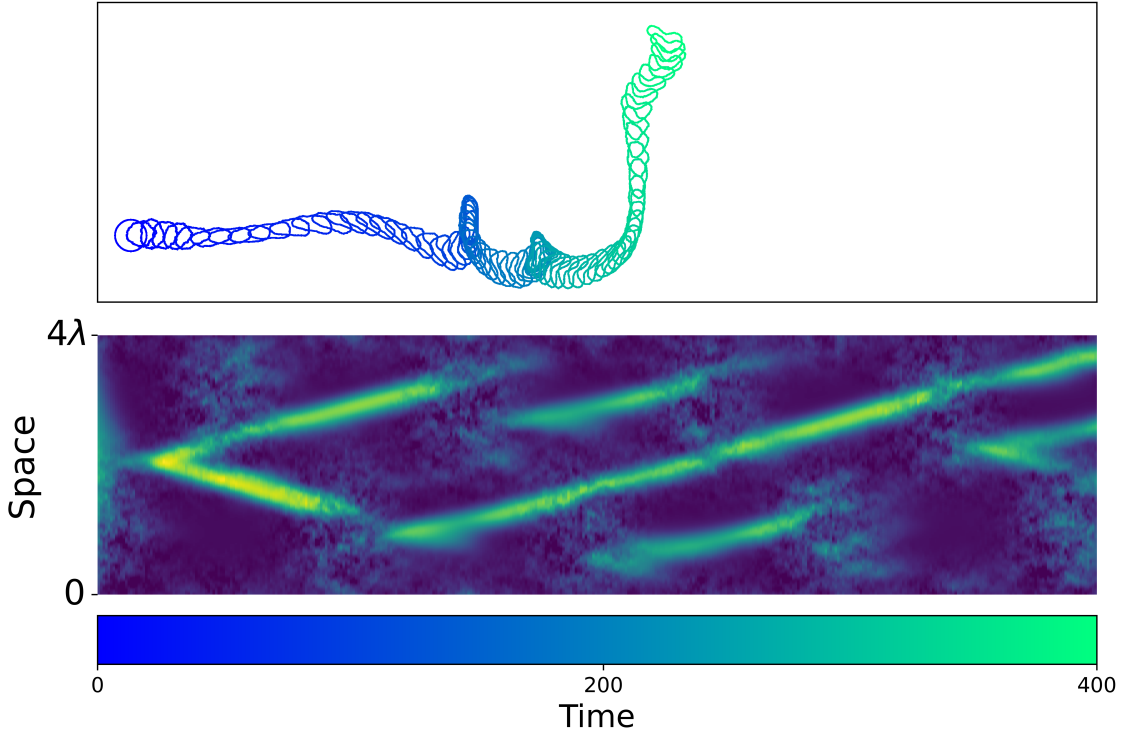


Figure 16: **Effect of continual noise.** A simulation, as in Figure 11, but with continual space-time distributed noise (18) that disrupts the counter-propagating peaks and $L = 4\lambda$. Random noise can cause one or the other pseudopod to “take over”, in a behavior resembling the Dictyostelium motility phenotype. Parameters as in Table I with $s = 0.8$. Initial conditions given by (17). Produced with Dictry.xml

numerical PDE bifurcation analysis of a system of active and inactive GTPase, and F-actin [27]. This basis helped us to find interesting regimes of parameters and understand how transitions in behavior depend on parameters. Among the parameters of interest, we chiefly investigated the F-actin dependent GTPase inactivation rate. The bifurcation analysis also allowed us to construct relevant simulation experiments and interpret the results.

The model (1) for the regulatory circuit described in Figure 1b is closely related to models for “actin waves” proposed and studied earlier [23, 32]. A few 2D CPM cell simulations were shown in [32], but here, we conducted a systematic study of how the PDE bifurcations lead to cell behavioral transitions. To do so, we simplified the representation of cells by retaining only their edge contours, and solved the reaction-diffusion PDEs on the cell edge using the Morpheus open-source software plugin for a membrane RD solver. Further, these simulations linked edge protrusion at each site to the magnitude of the F-actin variable F at that site. Retraction was implicitly computed from an area constraint in the CPM.

The simulations demonstrate a variety of “phenotypes”, such as directed motion of polar and wobbly cells, in situ ruffling of cells whose edge sustains traveling waves, cell turning, and pseudopod competition. The addition of stochasticity can also produce the less regular amoeboid behavior observed in *D. discoideum*. Of particular interest is the observation that a fixed set of parameters can result in coexisting motility modes (e.g. polar or ruffling cells), so that noise or input of some kind can cause transitions in cell behavior.

Our simulations and bifurcation analyses show that these different phenotypes and regimes of behavior are governed by key model parameters, and thus we can make predictions of the types of observed cell shapes and motility based on variation of these parameters. In particular, we observed that the width of the polar pattern, and thus the width of the leading edge, is inversely proportional to the F-actin-dependent inactivation rate, s . We also saw that lower values of s favor polarity and higher values favor turning and ruffling. The cell perimeter, L , or equivalently the diffusion rates of the GTPase and F-actin or the GTPase basal rate of inactivation (see Section A.2) also play an important role in the observed phenotypes. The transition between stable polarity and single-peak traveling waves, through the parity-breaking bifurcation, is only observed for a specific range of L . For L below this range, single-peak waves are observed but stable polarity is

absent.

The simplicity of the model and its simulations also mean that predictions have limitations. First, the membrane RD solvers in Morpheus do not take cell edge deformation into account: rather, the RD system is solved on the edge of a circular cell of equal area and mapped onto the deforming cell edge. Second, we do not control explicitly for membrane tension; the CPM perimeter constraint acts to limit edge expansion, but does not affect the signaling system. Finally, we assume that parameters are constant along the cell edge, whereas in real cells, the front and back likely become distinct, and prevent waves from circulating all around the cell. See, for example, lamellipodial waves in [7] that propagate only along the front part of the cell edge.

All in all, our paper emphasizes several key ideas: (1) Mathematical analysis of prototypical models for signaling can guide judicious exploration of model parameters and facilitate numerical exploration. (2) PDE bifurcation analysis can provide insights into coexistence of behaviors and how new behaviors emerge as parameters are tuned. (3) Relatively simple CPM simulations can provide a useful tool for exploratory simulations of the link between regulatory circuits and emergent cell behaviors.

Elsewhere [3], a similar computational approach was recently used to link proposed Rac signaling circuits to optogenetic experimental data for migrating neutrophils. Despite its limitations, the CPM simulation platform could readily capture realistic cell trajectories for many stimuli protocols. In future, we plan to investigate models for interacting GTPases (e.g., Rac-Rho), effects of membrane tension, and nonuniform environments to extend the realism of the modeling approach.

Acknowledgments:

We'd like to thank Arik Yochelis for helpful discussions and comments. This work was funded by a Natural Sciences and Engineering Research Council of Canada (NSERC) CGS-D Scholarship and Centre de Recherches Mathématiques and the Institut des Sciences Mathématiques postdoctoral fellowship awarded to JMH and an NSERC Discovery Grant to LEK.

Disclosure statement:

No potential conflict of interest is reported by the authors

A Model description and non-dimensionalization

A.1 Model for cell polarity

The model discussed in this work is a simplification of the Holmes model [23], which describes GTPase-actin dynamics using a set of three reaction-diffusion equations. His model is based on the cell polarization model by [41], which, in fully dimension-carrying form, is given by the set of PDEs

$$\frac{\partial u}{\partial t} = \left(\beta_0 + \gamma_0 \frac{u^2}{u_0^2 + u^2} \right) v - \delta_0 u + D_{u,0} \frac{\partial^2 u}{\partial x^2}, \quad (6a)$$

$$\frac{\partial v}{\partial t} = - \left(\beta_0 + \gamma_0 \frac{u^2}{u_0^2 + u^2} \right) v + \delta_0 u + D_{v,0} \frac{\partial^2 v}{\partial x^2}, \quad (6b)$$

where u, v are, respectively, active and inactive GTPases, β_0 is a basal rate of activation, δ_0 is an inactivation rate, γ_0 is the rate of auto-activation (positive feedback of active GTPase to accelerate its activation rate), u_0 is the “EC50” parameter, i.e., the GTPase level at which the Hill function feedback term is at its half maximum, and $D_{u,0} < D_{v,0}$ are the rates of diffusion for the active and inactive GTPase. Here the model assumes positive feedback onto the GEFs. See Appendix A in [29], which shows that negative feedback onto the GAPs is qualitatively the same. Typical boundary conditions are homogeneous Neumann or periodic. This model conserves mass:

$$G_T := \frac{1}{L} \int_0^L [u(x, t) + v(x, t)] dz = \text{constant}, \quad (7)$$

where $(0, L)$ is the spatial domain and L denotes the perimeter of the cell. The mass is normalized by the domain length and thus $L \cdot G_T$ denotes the total, conserved amount of GTPase in the system. The advantage of starting with this form of the model (6) is that we know the interpretation and units of all the basic parameters. Namely, $\beta_0, \gamma_0, \delta_0$ have units of 1/time, u, v, u_0 have units of GTPase concentration, and $D_{u,0}$ and $D_{v,0}$ have units of length²/time.

A.2 Non-dimensionalization and coupling F-actin

We rewrite the reaction kinetics by rescaling the Hill function

$$f(u, v) := \left(\beta_0 + \gamma_0 \frac{u^2}{u_0^2 + u^2} \right) v - \delta_0 u = \left(\beta_0 + \gamma_0 \frac{(u/u_0)^2}{1 + (u/u_0)^2} \right) v - \delta_0 u,$$

to have a dimensionless numerator and denominator. The polynomial variant of (6), used as the “wave-pinning” subsystem in our model (1), is obtained by multiplying kinetic terms by the dimensionless denominator $(1 + (u/u_0)^2)$, obtaining the new PDEs

$$\frac{\partial u}{\partial t} = (\beta_0 + \gamma_1 (u/u_0)^2) v - \delta_0 (1 + (u/u_0)^2) u + D_{u,0} \frac{\partial^2 u}{\partial x^2}, \quad (8a)$$

$$\frac{\partial v}{\partial t} = -(\beta_0 + \gamma_1 (u/u_0)^2) v + \delta_0 (1 + (u/u_0)^2) u + D_{v,0} \frac{\partial^2 v}{\partial x^2}, \quad (8b)$$

where $\gamma_1 = (\beta_0 + \gamma_0)$. Analogously to the derivation of the Holmes model [23], we add the effect of F-actin to arrive at a dimensional PDE

$$\frac{\partial u}{\partial t} = (\beta_0 + \gamma_1 (u/u_0)^2) v - \delta_0 (1 + (u/u_0)^2 + \sigma F) u + D_{u,0} \frac{\partial^2 u}{\partial x^2}.$$

where $\delta_0 \sigma$ is the F-actin dependent GTPase inactivation rate. To nondimensionalize, we define

$$u^* := \frac{u}{u_0}, \quad v^* = \frac{v}{u_0}, \quad F^* = \frac{F}{F_0}, \quad t^* = \delta t, \quad x^* = \frac{x}{L}$$

where * 's denote dimensionless variables and F_0 is the scale for F . Note that u and v have the same scale. Substituting into the model PDEs (8) and simplifying yields

$$\frac{\partial u^*}{\partial t^*} = (b + \gamma(u^*)^2) v^* - (1 + (u^*)^2 + sF) u + D_u \frac{\partial^2 u^*}{\partial (x^*)^2}, \quad (9a)$$

$$\frac{\partial v^*}{\partial t^*} = - (b + \gamma(u^*)^2) v^* + (1 + (u^*)^2 + sF) u + D_v \frac{\partial^2 v^*}{\partial (x^*)^2}, \quad (9b)$$

where

$$b := \frac{\beta_0}{\delta_0}, \quad \gamma := \frac{\gamma_1}{\delta_0} = \frac{\beta_0 + \gamma_0}{\delta_0}, \quad s := \sigma F_0, \quad D_u := \frac{D_{u,0}}{\delta_0 L^2}, \quad D_v := \frac{D_{v,0}}{\delta_0 L^2},$$

are dimensionless parameters. In the rescaled variables, mass conservation becomes

$$\int_0^1 [u^*(x^*, t^*) + v^*(x^*, t^*)] dx^* = \frac{G_T}{u_0} =: M.$$

In [27], the original paper that introduced the model we study (1), the scale for F was not selected and the equation governing F-actin was given by

$$\frac{dF^*}{dt^*} = \omega(p_0 + p_1 u^* - F^*) + D_F \frac{\partial^2 F^*}{\partial (x^*)^2}, \quad (10)$$

where

$$\omega := \frac{\theta}{\delta_0}, \quad p_0 := \frac{\rho_0}{F_0 \theta}, \quad p_1 := \frac{\rho_1 u_0}{F_0 \theta}, \quad D_F := \frac{D_{F,0}}{\delta_0 L^2}.$$

are the dimensionless parameters with $F_0 = 1$. The dimensional parameters ρ_0, ρ_1, θ denote the basal and GTPase dependent F-actin assembly rate, and the F-actin disassembly rate, respectively. Dropping the * 's and combining (9) and (10) yields our GTPase-actin model (1)

A.3 Biological correspondence

The basic interactions of Figure 1b were found experimentally in [9, 21, 31, 39, 51], and modeled in a similar spirit in these and companion papers. In this system, the GTPase is RhoA, and F-actin its downstream effector. Rho activates its own GEF, Ect2. Rho promotes F-actin through the formin (mDia) and F-actin recruits the GAP RGA3/4 that inactivates RhoA.

While the model in the above papers differs from ours in various details, the basic features are quite similar. We can identify our parameter b as a basal rate and γ as the Ect2-dependent Rho activation rate (Rho self-activates via Ect2). The parameter s would be the RGA3/4-dependent Rho inactivation rate, which is assumed to be proportional to the level of F-actin. The total Rho (active plus inactive) is M .

B Cellular Potts model computations

The cellular Potts model (CPM) is a lattice-based simulation where a single cell is represented by a connected subset of lattice sites (“pixels”) with an ID=1. Sites outside the cell (denoted “medium”) are labeled with ID=0. Cell expansion and retraction can occur along the edge of this cell. In its simplest form, the algorithm proceeds as follows:

1. Choose a random lattice site i .
2. Choose a random neighboring lattice site j and propose to copy the ID from i to j .
3. Calculate the difference in “free energy,” ΔH , between the current and proposed new configuration, where the Hamiltonian, H , is given by

$$H = \lambda_a(A - A_0)^2 + \lambda_p(P - P_0)^2$$

with A, A_0, λ_a being the current area, target area, and area constraint weight, and similarly for the perimeter P .

4. Accept or reject the new configuration according to the following rule:
 - If $\Delta H \leq 0$, accept;
 - If $\Delta H > 0$, then accept the new configuration with a probability $e^{-\Delta H/T}$, where T is the Boltzmann temperature parameter.

While the canonical CPM selects sites randomly from the entire lattice, Morpheus [49], the software package we use, optimizes this by selecting only sites at the boundaries between cell and medium where configuration changes can occur. In our implementation, we also apply the perimeter constraint using an “asphericity” parameter, which instead computes the perimeter relative to that of a circle with the same area as the CPM cell. The area constraint implies that cell protrusion along part of the edge is inherently balanced by a tendency to retract other parts of the cell and the perimeter constraint acts as an effective “membrane tension” or stiffness that governs overall cell shape.

To capture the effects of F-actin on cell shape and motility, the PDEs (1) are solved at each point on the CPM cell edge. Updates to the CPM simulation that protrude the cell edge at x , a location along the cell edge, are favored if the value of F-actin, $F(x, t)$, is high. This results in an additional term added to the Hamiltonian. For each simulation, the cell is initiated as a circle.

C More bifurcation diagrams and parameter sweeps

Here, we present additional bifurcation diagrams and another parameter sweep. Figure 17 shows all stationary solutions emerging from the HSSs when $L = 3\lambda$ and the traveling wave solutions with the same wavelength. We include this figure to demonstrate that traveling waves with different wavelengths also exist/coexist and only unipolar patterns are stable. In Figure 18 we show a similar structure when $L = 2\lambda$.

In Figure 19, we show a parameter sweep as in Figure 3, but with $L = 2\lambda$. Polar, traveling wave, and time-periodic solutions resembling counter-propagating waves are still observed; however, unlike the $L = 3\lambda$ case, there are no transient interactions with these solutions.

D Simulation details

Unless otherwise stated, we used parameter values given in Table I with $b = 0.067$.

Figure 7: Domain length: $L = 3\lambda$, where $\lambda \approx 3.09$ is the numerically solved for wavelength that leads to the WB of the codimension-2 LW/WB. The three simulations use the s values 0.376, 0.475, 0.519.

Initial conditions:

$$u(x, 0) = 0.75 - 0.5 \cos(x), \quad (11a)$$

$$v(x, 0) = 1.25 + 0.1 \cos(x), \quad (11b)$$

$$F(x, 0) = 3.5 - 2 \cos(x). \quad (11c)$$

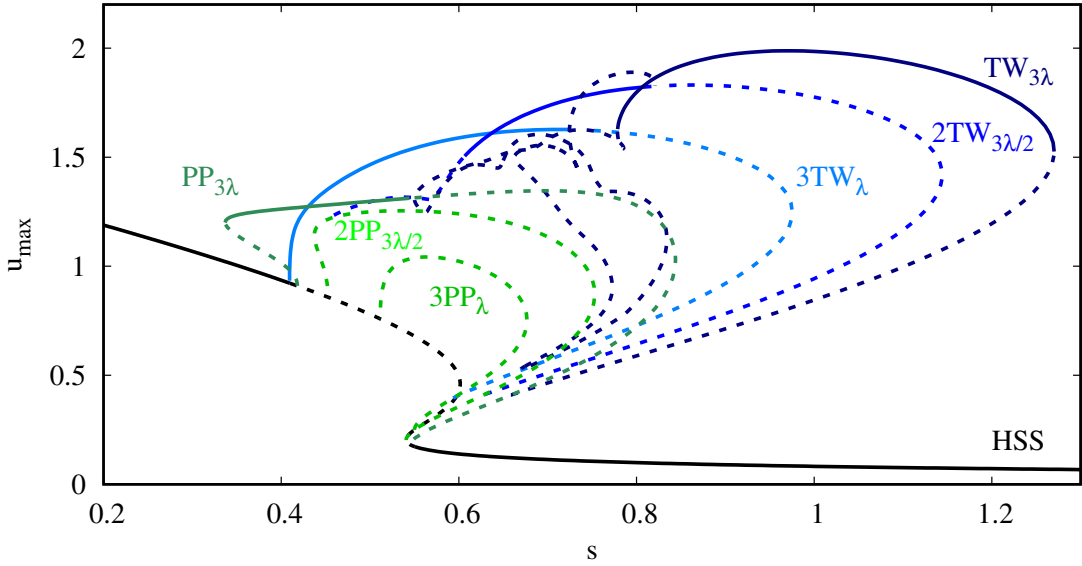


Figure 17: **Polar and traveling waves of various wavelength:** As in Figure 5 but showcasing traveling waves (TWs) and polar patterns (PPs) with wavelengths λ , $3\lambda/2$ and 3λ . The notation $3TW_\lambda$ denotes TWs with wavelength λ and three spatial copies. This figure shows part of the bifurcation structure for simulations in Figures 7 to 9. The traveling wave solutions represent cell turning ($TW_{3\lambda}$) and ruffling ($2TW_{3\lambda/2}$ and $3TW_\lambda$). The polar solutions $PP_{3\lambda}$, $2PP_{3\lambda/2}$, and $3PP_\lambda$ represent polar, bipolar, and tripolar solutions, respectively. However, as before, only stable solutions (solid branches) are biologically observable.

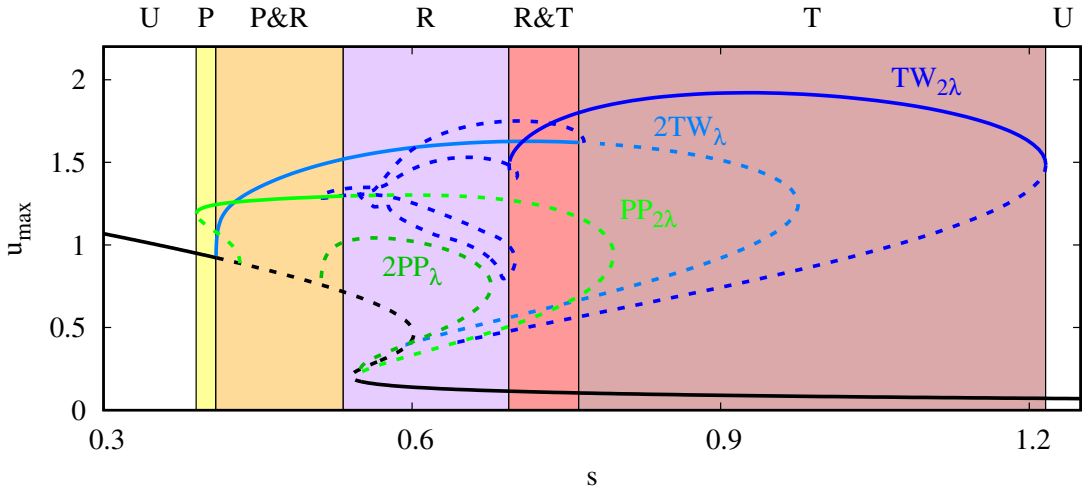


Figure 18: **Coexistence of polar and ruffling states in smaller cells:** Single parameter bifurcation diagram as in Figure 17 but with $L = 2\lambda$. This figure shows part of the bifurcation structure for simulations in Figures 10 and 11. Here, we show unipolar ($PP_{2\lambda}$) and bipolar ($2PP_\lambda$) solutions, and traveling waves with 1 peak ($TW_{2\lambda}$, “turning”) and 2 peaks ($2TW_\lambda$, “ruffling”). The shaded regions denote various existence and coexistence regimes of nonlinear patterns: yellow - polarization (P), orange - polarization and ruffling (P&R), purple - ruffling (R), red - ruffling and turning (R&T), and brown - turning (T). Cell turning with a perimeter $L = 2\lambda$ is shown in the top panel of Figure 11.

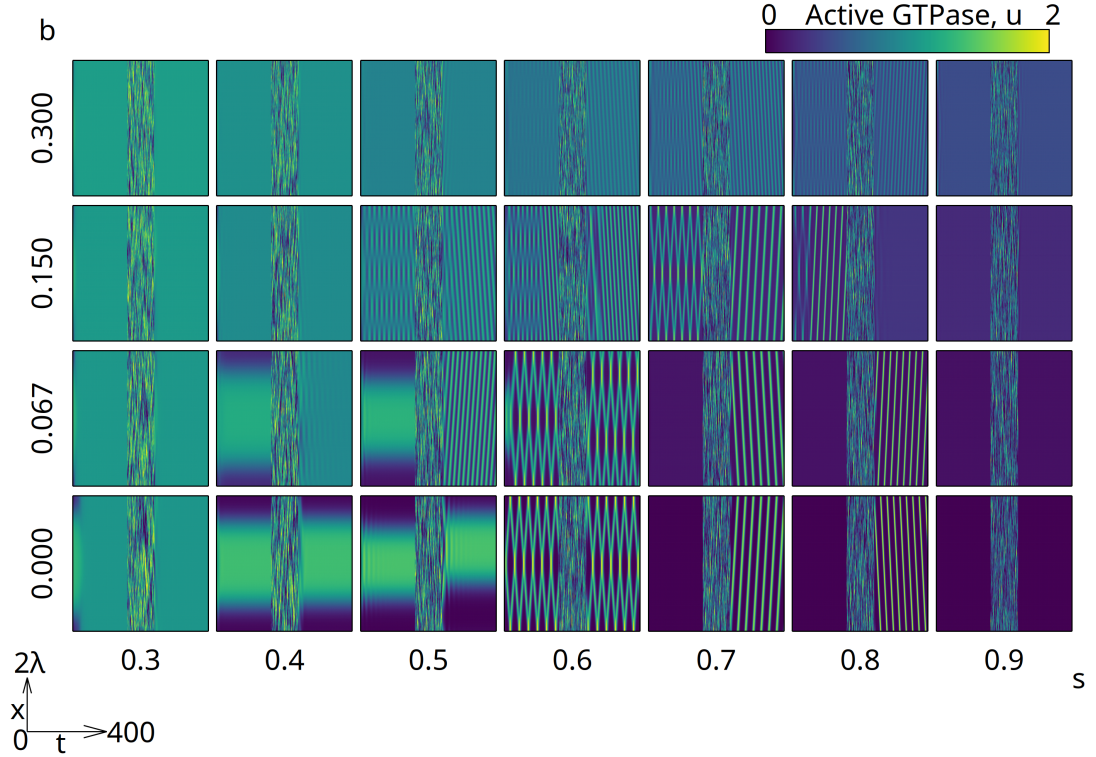


Figure 19: **Parameter sweep with $L = 2\lambda$:** As in Figure 3 but with $L = 2\lambda$. When $L = 2\lambda$, time-periodic solutions resembling counter-propagating waves and coexistence of polar and traveling wave solutions are still observed. Other parameter values as in Table I.

Table I: **Model parameter values:** Dimensionless parameter values used in simulations

| Parameter | Definition | Value |
|-----------|--------------------------------------|-------------|
| b | GTPase basal activation rate | varied |
| γ | GTPase feedback activation rate | 3.557 |
| s | F-actin dependent inactivation rate | varied |
| ω | F-actin time scale parameter | 0.6 |
| p_0 | F-actin basal growth rate | 0.8 |
| p_1 | GTPase dependent F-actin growth rate | 3.8 |
| L | Cell perimeter | varied |
| D_u | Active GTPase diffusion rate | $0.1/L^2$ |
| D_v | Inactive GTPase diffusion rate | $1/L^2$ |
| D_F | F-actin diffusion rate | $0.001/L^2$ |
| M | Average GTPase density | 2 |

Figure 8: Domain length: $L = 3\lambda$ and s values 0.413, 0.475, 0.607.

Initial conditions:

$$u(x, 0) = 1 - 0.5 \cos(3x) - 0.32 \sin(3x), \quad (12a)$$

$$v(x, 0) = 1 + 0.028 \cos(3x) + 0.08 \sin(3x), \quad (12b)$$

$$F(x, 0) = 4.6 - 2 \cos(3x). \quad (12c)$$

Figure 9: Same initial conditions, domain length, and parameters as for Figure 7, but with $s = 0.54$.

Figure 10: Domain length: $L = 2\lambda$ and $s = 0.6$.

Initial conditions:

$$u(x, 0) = 0.75 - 0.5 \cos(x), \quad (13a)$$

$$v(x, 0) = 1.25 + 0.1 \cos(x), \quad (13b)$$

$$F(x, 0) = 3.5 - 2 \cos(x). \quad (13c)$$

Figure 11: Same initial conditions, domain length, and parameter values as for Figure 10 but with $s = 0.8$ and noise added to the GTPase equations for $150 \leq t \leq 200$. In particular, we added Noise:

$$\xi(x, t) = 4\mathcal{N},$$

where \mathcal{N} is a standard normal random number at each grid and time point. The noise was implemented as follows:

$$\frac{du}{dt} = (b + \gamma u^2)v - (1 + sF + u^2)u + D\Delta u + \xi(x, t), \quad (14a)$$

$$\frac{dv}{dt} = -(b + \gamma u^2)v + (1 + sF + u^2)u + \Delta v - \xi(x, t). \quad (14b)$$

to maintain mass conservation.

Figure 12: Domain length: $L = 5$.

Parameter values as in Table I, but with a time-dependent F-actin dependent inactivation rate, with parameters $s_0 = 0.475$ and $s_f = 0.6$

$$s(t) = \begin{cases} s_0 & t < 125, \\ s_0 - (s_0 - s_f)(t - 125)/250 & 125 \leq t \leq 375, \\ s_f & t > 375. \end{cases} \quad (15)$$

Initial conditions given by (13).

Figure 13: Same domain length and parameters as for Figure 12 but with the starting and ending values of s interchanged, i.e., $s_0 = 0.6$ and $s_f = 0.475$.

Initial conditions:

$$u(x, 0) = 0.07 + 2\operatorname{sech}(3(x - L/2)), \quad (16a)$$

$$v(x, 0) = M - u(x, 0), \quad (16b)$$

$$F(x, 0) = 1.15 + 5\operatorname{sech}(3(x - L/3)), \quad (16c)$$

where $M = 2$.

Figure 14: Same domain length, parameters, and initial conditions as for Figure 12 but with s changing randomly in time within the interval $[0.475, 0.6]$ (see the xml file for implementation details Dicty.xml).

Figure 16: Domain length: $L = 4\lambda$ and $s = 0.8$.

Initial conditions:

$$u(x, 0) = 1 - 0.5 \cos(x), \quad (17a)$$

$$v(x, 0) = 1 + 0.1 \cos(x), \quad (17b)$$

$$F(x, 0) = 4.5 - 0.82 \cos(x). \quad (17c)$$

Continual spatiotemporal noise was added similarly to Figure 11 but of the form

$$\xi(x, t) = 2[(1 + \sin(x))((1 - \cos(6.5t/100))^2) + (1 - \sin(x))(1 + \cos(6.5t/100))^2]\mathcal{N}, \quad (18)$$

where \mathcal{N} is a standard normal random number at each grid and time point. The noise was then added and subtracted to the active and inactive GTPase equations as in (14).

References

- [1] R. ALERT AND X. TREPAT, *Physical models of collective cell migration*, Annu. Rev. Condens. Matter Phys., 11 (2020), pp. 77–101, doi:10.1146/annurev-conmatphys-031218-013516.
- [2] J. ALGORTA, A. FELE-PARANJ, J. M. HUGHES, AND L. EDELSTEIN-KESHET, *Modeling and simulating single and collective cell motility*, Cold Spring Harb. Perspect. Biol., 17 (2025), a041796, doi:10.1101/cshperspect.a041796.
- [3] J. ALGORTA, J. P. TOWN, O. D. WEINER, AND L. EDELSTEIN-KESHET, *Investigating local negative feedback of Rac activity by mathematical models and cell motility simulations*, iScience, (2026), 114641, doi:10.1016/j.isci.2026.114641.
- [4] J. ALLARD AND A. MOGILNER, *Traveling waves in actin dynamics and cell motility*, Curr. Opin. Cell Biol., 25 (2013), pp. 107–115, doi:10.1016/j.ceb.2012.08.012.
- [5] S. ALONSO, M. STANGE, AND C. BETA, *Modeling random crawling, membrane deformation and intracellular polarity of motile amoeboid cells*, PloS One, 13 (2018), e0201977, doi:10.1371/journal.pone.0201977.
- [6] Y. ARAI, T. SHIBATA, S. MATSUOKA, M. J. SATO, T. YANAGIDA, AND M. UEDA, *Self-organization of the phosphatidylinositol lipids signaling system for random cell migration*, Proc. Natl. Acad. Sci. USA, 107 (2010), pp. 12399–12404, doi:10.1073/pnas.0908278107.
- [7] E. L. BARNHART, J. ALLARD, S. S. LOU, J. A. THERIOT, AND A. MOGILNER, *Adhesion-dependent wave generation in crawling cells*, Curr. Biol., 27 (2017), pp. 27–38, doi:10.1016/j.cub.2016.11.011.
- [8] W. M. BEMENT, A. B. GORYACHEV, A. L. MILLER, AND G. VON DASSOW, *Patterning of the cell cortex by Rho GTPases*, Nat. Rev. Mol. Cell Biol., 25 (2024), pp. 290–308, doi:10.1038/s41580-024-00701-7.
- [9] W. M. BEMENT, M. LEDA, A. M. MOE, A. M. KITA, M. E. LARSON, A. E. GOLDING, C. PFEUTI, K.-C. SU, A. L. MILLER, A. B. GORYACHEV, ET AL., *Activator–inhibitor coupling between Rho signalling and actin assembly makes the cell cortex an excitable medium*, Nat. Cell Biol., 17 (2015), pp. 1471–1483, doi:10.1038/ncb3251.
- [10] E. BERNITT, H.-G. DÖBEREINER, N. S. GOV, AND A. YOCHELIS, *Fronts and waves of actin polymerization in a bistability-based mechanism of circular dorsal ruffles*, Nat. Commun., 8 (2017), 15863, doi:10.1038/ncomms15863.
- [11] C. BETA, L. EDELSTEIN-KESHET, N. GOV, AND A. YOCHELIS, *From actin waves to mechanism and back: How theory aids biological understanding*, eLife, 12 (2023), e87181, doi:10.7554/eLife.87181.
- [12] C. BETA AND K. KRUSE, *Intracellular oscillations and waves*, Annu. Rev. Condens. Matter Phys., 8 (2017), pp. 239–264, doi:10.1146/annurev-conmatphys-031016-025210.
- [13] A. BUTTENSCHÖN AND L. EDELSTEIN-KESHET, *Bridging from single to collective cell migration: A review of models and links to experiments*, PLoS Comput. Biol., 16 (2020), e1008411, doi:10.1371/journal.pcbi.1008411.

- [14] B. A. CAMLEY AND W.-J. RAPPEL, *Physical models of collective cell motility: from cell to tissue*, J. Phys. D: Appl. Phys., 50 (2017), 113002, doi:10.1088/1361-6463/aa56fe.
- [15] B. A. CAMLEY, Y. ZHAO, B. LI, H. LEVINE, AND W.-J. RAPPEL, *Crawling and turning in a minimal reaction-diffusion cell motility model: Coupling cell shape and biochemistry*, Phys. Rev. E, 95 (2017), 012401, doi:10.1103/PhysRevE.95.012401.
- [16] D. CUSSEDDU, L. EDELSTEIN-KESHET, J. MACKENZIE, S. PORTET, AND A. MADZVAMUSE, *A coupled bulk-surface model for cell polarisation*, J. Theor. Biol., 481 (2019), pp. 119–135, doi:10.1016/j.jtbi.2018.09.008.
- [17] H.-G. DÖBEREINER, B. J. DUBIN-THALER, J. M. HOFMAN, H. S. XENIAS, T. N. SIMS, G. GIANNONE, M. L. DUSTIN, C. H. WIGGINS, AND M. P. SHEETZ, *Lateral membrane waves constitute a universal dynamic pattern of motile cells*, Phys. Rev. Lett., 97 (2006), p. 038102, doi:10.1103/PhysRevLett.97.038102.
- [18] C. M. ELLIOTT, B. STINNER, AND C. VENKATARAMAN, *Modelling cell motility and chemotaxis with evolving surface finite elements*, J. R. Soc. Interface, 9 (2012), p. 3027–3044, doi:10.1098/rsif.2012.0276.
- [19] G. GERISCH, M. ECKE, B. SCHROTH-DIEZ, S. GERWIG, U. ENGEL, L. MADDERA, AND M. CLARKE, *Self-organizing actin waves as planar phagocytic cup structures*, Cell. Adh. Migr., 3 (2009), pp. 373–382, doi:10.4161/cam.3.4.9708.
- [20] G. GIANNONE, B. J. DUBIN-THALER, H.-G. DÖBEREINER, N. KIEFFER, A. R. BRESNICK, AND M. P. SHEETZ, *Periodic lamellipodial contractions correlate with rearward actin waves*, Cell, 116 (2004), pp. 431–443, doi:10.1016/s0092-8674(04)00058-3.
- [21] A. B. GORYACHEV, M. LEDA, A. L. MILLER, G. von DASSOW, AND W. M. BEMENT, *How to make a static cytokinetic furrow out of traveling excitable waves*, Small GTPases, 7 (2016), pp. 65–70, doi:10.1080/21541248.2016.1168505.
- [22] F. GRANER AND J. A. GLAZIER, *Simulation of biological cell sorting using a two-dimensional extended potts model*, Phys. Rev. Lett., 69 (1992), pp. 2013—2016, doi:10.1103/physrevlett.69.2013.
- [23] W. R. HOLMES, A. E. CARLSSON, AND L. EDELSTEIN-KESHET, *Regimes of wave type patterning driven by refractory actin feedback: transition from static polarization to dynamic wave behaviour*, Phys. Biol., 9 (2012), 046005, doi:10.1088/1478-3975/9/4/046005.
- [24] W. R. HOLMES AND L. EDELSTEIN-KESHET, *A comparison of computational models for eukaryotic cell shape and motility*, PLoS Comput. Biol., 8 (2012), e1002793, doi:10.1371/journal.pcbi.1002793.
- [25] J. M. HUGHES, *Numerical bifurcation study of a mass conserved reaction-diffusion model for actin waves: Unravelling motility modes of cells*, PhD thesis, University of British Columbia, Nov 2025.
- [26] J. M. HUGHES, C. MARTINEZ-TORRES, C. BETA, L. EDELSTEIN-KESHET, AND A. YOCHELIS, *A dissipative mass conserved reaction-diffusion system reveals switching between coexisting polar and oscillatory cell motility states*, Chaos, 35 (2025), 051103, doi:10.1063/5.0274689.
- [27] J. M. HUGHES, S. MODAI, L. EDELSTEIN-KESHET, AND A. YOCHELIS, *Travelling waves and wave pinning (polarity): Switching between random and directional cell motility*, SIAM J. Appl. Dyn. Syst., (2026).
- [28] R. H. INSALL, *Understanding eukaryotic chemotaxis: a pseudopod-centred view*, Nat. Rev. Mol. Cell Biol., 11 (2010), pp. 453–458, doi:10.1038/nrm2905.
- [29] A. JILKINE, A. F. MARÉE, AND L. EDELSTEIN-KESHET, *Mathematical model for spatial segregation of the Rho-family GTPases based on inhibitory crosstalk*, Bull. Math. Biol., 69 (2007), pp. 1943–1978, doi:10.1007/s11538-007-9200-6.
- [30] E. KNOBLOCH, *Oscillatory convection in binary mixtures*, Phys. Rev. A, 34 (1986), 1538, doi:10.1103/PhysRevA.34.1538.

[31] J. LANDINO, M. LEDA, A. MICHAUD, Z. T. SWIDER, M. PROM, C. M. FIELD, W. M. BEMENT, A. G. VECCHIARELLI, A. B. GORYACHEV, AND A. L. MILLER, *Rho and F-actin self-organize within an artificial cell cortex*, *Curr. Biol.*, 31 (2021), pp. 5613–5621, doi:10.1016/j.cub.2021.10.021.

[32] Y. LIU, E. G. RENS, AND L. EDELSTEIN-KESHET, *Spots, stripes, and spiral waves in models for static and motile cells*, *J. Math. Biol.*, 82 (2021), pp. 1–38, doi:10.1007/s00285-021-01550-0.

[33] M. MACHACEK AND G. DANUSER, *Morphodynamic profiling of protrusion phenotypes*, *Biophys. J.*, 90 (2006), pp. 1439–1452, doi:10.1529/biophysj.105.070383.

[34] M. MACHACEK, L. HODGSON, C. WELCH, H. ELLIOTT, O. PERTZ, P. NALBANT, A. ABELL, G. L. JOHNSON, K. M. HAHN, AND G. DANUSER, *Coordination of Rho GTPase activities during cell protrusion*, *Nature*, 461 (2009), pp. 99–103, doi:10.1038/nature08242.

[35] A. F. MARÉE, V. A. GRIENEISEN, AND L. EDELSTEIN-KESHET, *How cells integrate complex stimuli: the effect of feedback from phosphoinositides and cell shape on cell polarization and motility*, *PLoS Comput. Biol.*, 8 (2012), e1002402, doi:10.1371/journal.pcbi.1002402.

[36] O. MAXIAN, A. R. DINNER, AND E. MUNRO, *Actin network heterogeneity tunes activator-inhibitor dynamics at the cell cortex*, *Proc. Natl. Acad. Sci. U S A*, 122 (2025), e2520485122, doi:10.1073/pnas.2520485122.

[37] F. MERINO-CASALLO, M. J. GOMEZ-BENITO, S. HERVAS-RALUY, AND J. M. GARCIA-AZNAR, *Unravelling cell migration: defining movement from the cell surface*, *Cell Adhes. Migr.*, 16 (2022), pp. 25–64, doi:10.1080/19336918.2022.2055520.

[38] A. MICHAUD, M. LEDA, Z. T. SWIDER, S. KIM, J. HE, J. LANDINO, J. R. VALLEY, J. HUISKEN, A. B. GORYACHEV, G. VON DASSOW, ET AL., *A versatile cortical pattern-forming circuit based on Rho, F-actin, Ect2 and RGA-3/4*, *J. of Cell Biol.*, 221 (2022), e202203017, doi:10.1083/jcb.202203017.

[39] A. MICHAUD, Z. T. SWIDER, J. LANDINO, M. LEDA, A. L. MILLER, G. VON DASSOW, A. B. GORYACHEV, AND W. M. BEMENT, *Cortical excitability and cell division*, *Curr. Biol.*, 31 (2021), pp. R553–R559, doi:10.1016/j.cub.2021.02.053.

[40] T. MOLDENHAWER, E. MORENO, D. SCHINDLER, S. FLEMMING, M. HOLSCHEIDER, W. HUISINGA, S. ALONSO, AND C. BETA, *Spontaneous transitions between amoeboid and keratocyte-like modes of migration*, *Front. Cell Dev. Biol.*, 10 (2022), 898351, doi:10.3389/fcell.2022.898351.

[41] Y. MORI, A. JILKINE, AND L. EDELSTEIN-KESHET, *Wave-pinning and cell polarity from a bistable reaction-diffusion system*, *Biophys. J.*, 94 (2008), pp. 3684–3697, doi:10.1529/biophysj.107.120824.

[42] M. P. NEILSON, J. A. MACKENZIE, S. D. WEBB, AND R. H. INSALL, *Modeling cell movement and chemotaxis using pseudopod-based feedback*, *SIAM J. Sci. Comput.*, 33 (2011), pp. 1035–1057, doi:10.1137/100788938.

[43] M. P. NEILSON, D. M. VELTMAN, P. J. VAN HAASTERT, S. D. WEBB, J. A. MACKENZIE, AND R. H. INSALL, *Chemotaxis: A feedback-based computational model robustly predicts multiple aspects of real cell behaviour*, *PLoS Biol.*, 9 (2011), e1000618, doi:10.1371/journal.pbio.1000618.

[44] E. G. RENS AND L. EDELSTEIN-KESHET, *Cellular tango: How extracellular matrix adhesion choreographs Rac-Rho signaling and cell movement*, *Phys. Biol.*, 18 (2021), 066005, doi:10.1088/1478-3975/ac2888.

[45] D. SCHINDLER, T. MOLDENHAWER, M. STANGE, V. LEPRO, C. BETA, M. HOLSCHEIDER, AND W. HUISINGA, *Analysis of protrusion dynamics in amoeboid cell motility by means of regularized contour flows*, *PLoS Comput. Biol.*, 17 (2021), p. e1009268, doi:10.1371/journal.pcbi.1009268.

[46] D. SHAO, H. LEVINE, AND W.-J. RAPPEL, *Coupling actin flow, adhesion, and morphology in a computational cell motility model*, *Proc. Natl. Acad. Sci. U S A*, 109 (2012), pp. 6851–6856, doi:10.1073/pnas.1203252109.

[47] D. SPANO, C. HECK, P. DE ANTONELLIS, G. CHRISTOFORI, AND M. ZOLLO, *Molecular networks that regulate cancer metastasis*, Semin. Cancer Biol., 22 (2012), pp. 234—249, doi:10.1016/j.semancer.2012.03.006.

[48] C.-P. SPATARELU, H. ZHANG, D. T. NGUYEN, X. HAN, R. LIU, Q. GUO, J. NOTBOHM, J. FAN, L. LIU, AND Z. CHEN, *Biomechanics of collective cell migration in cancer progression: Experimental and computational methods*, ACS Biomater. Sci. Eng., 5 (2019), pp. 3766—3787, doi:10.1021/acsbiomaterials.8b01428.

[49] J. STARRUSS, W. DE BACK, L. BRUSCH, AND A. DEUTSCH, *Morpheus: a user-friendly modeling environment for multiscale and multicellular systems biology*, Bioinformatics, 30 (2014), pp. 1331–1332, doi:10.1093/bioinformatics/btt772.

[50] M. SUN AND M. H. ZAMAN, *Modeling, signaling and cytoskeleton dynamics: integrated modeling-experimental frameworks in cell migration*, WIREs Syst. Biol. Med., 9 (2016), e1365, doi:10.1002/wsbm.1365.

[51] Z. T. SWIDER, A. MICHAUD, M. LEDA, J. LANDINO, A. B. GORYACHEV, AND W. M. BEMENT, *Cell cycle and developmental control of cortical excitability in Xenopus laevis*, Mol. Biol. Cell, 33 (2022), ar73, doi:10.1091/mbc.E22-01-0025.

[52] J. P. TOWN AND O. D. WEINER, *Local negative feedback of Rac activity at the leading edge underlies a pilot pseudopod-like program for amoeboid cell guidance*, PLOS Biol., 21 (2023), e3002307, doi:10.1371/journal.pbio.3002307.

[53] N. VERSCHUEREN AND A. CHAMPNEYS, *A model for cell polarization without mass conservation*, SIAM J. Appl. Dyn. Syst., 16 (2017), pp. 1797–1830, doi:10.1137/16M1093847.

[54] M. G. VICKER, *F-actin assembly in Dictyostelium cell locomotion and shape oscillations propagates as a self-organized reaction-diffusion wave*, FEBS Lett., 510 (2002), pp. 5–9, doi:10.1016/S0014-5793(01)03207-0.

[55] O. D. WEINER, G. SERVANT, M. D. WELCH, T. J. MITCHISON, J. W. SEDAT, AND H. R. BOURNE, *Spatial control of actin polymerization during neutrophil chemotaxis*, Nat. Cell Biol., 1 (1999), pp. 75–81, doi:10.1038/10042.

[56] H. WEYER, F. BRAUNS, AND E. FREY, *Coarsening and wavelength selection far from equilibrium: A unifying framework based on singular perturbation theory*, Phys. Rev. E, 108 (2023), 064202, doi:10.1103/PhysRevE.108.064202.

[57] D. WINTERBOTTOM, P. MATTHEWS, AND S. COX, *Oscillatory pattern formation with a conserved quantity*, Nonlinearity, 18 (2005), 1031, doi:10.1088/0951-7715/18/3/006.

[58] K. WONG, O. PERTZ, K. HAHN, AND H. BOURNE, *Neutrophil polarization: spatiotemporal dynamics of RhoA activity support a self-organizing mechanism*, Proc. Natl. Acad. Sci. U S A, 103 (2006), pp. 3639–3644, doi:10.1073/pnas.0600092103.

[59] T. D. YANG, K. PARK, J.-S. PARK, J.-H. LEE, E. CHOI, J. LEE, W. CHOI, Y. CHOI, AND K. J. LEE, *Two distinct actin waves correlated with turns-and-runs of crawling microglia*, PLoS One, 14 (2019), e0220810, doi:10.1371/journal.pone.0220810.

[60] Y. YANG AND M. WU, *Rhythmicity and waves in the cortex of single cells*, Philos. Trans. R. Soc. Lond. B. Biol. Sci., 373 (2018), 20170116, doi:10.1098/rstb.2017.0116.

[61] A. YOCHELIS, S. FLEMMING, AND C. BETA, *Versatile patterns in the actin cortex of motile cells: Self-organized pulses can coexist with macropinocytic ring-shaped waves*, Phys. Rev. Lett., 129 (2022), 088101, doi:10.1103/PhysRevLett.129.088101.